

# REPORT DOCUMENTATION PAGE

*Form Approved*  
OMB No. 0704-0188

The public reporting burden for this collection of information is estimated to average 1 hour per response, including the time for reviewing instructions, searching existing data sources, gathering and maintaining the data needed, and completing and reviewing the collection of information. Send comments regarding this burden estimate or any other aspect of this collection of information, including suggestions for reducing this burden, to Department of Defense, Washington Headquarters Services, Directorate for Information Operations and Reports (0704-0188), 1215 Jefferson Davis Highway, Suite 1204, Arlington, VA 22202-4302. Respondents should be aware that notwithstanding any other provision of law, no person shall be subject to any penalty for failing to comply with a collection of information if it does not display a currently valid OMB control number. **PLEASE DO NOT RETURN YOUR FORM TO THE ABOVE ADDRESS.**

<b>1. REPORT DATE (DD-MM-YY)</b> September 2012			<b>2. REPORT TYPE</b> Final			<b>3. DATES COVERED (From - To)</b> 01 May 2009 – 30 April 2012		
<b>4. TITLE AND SUBTITLE</b> The Physics of Boundary-Layer Aero-Optic Effects						<b>5a. CONTRACT NUMBER</b>		
						<b>5b. GRANT NUMBER</b> FA9550-09-1-0449		
						<b>5c. PROGRAM ELEMENT NUMBER</b>		
<b>6. AUTHOR(S)</b> Stanislav Gordeyev and Eric J. Jumper (University of Notre Dame)						<b>5d. PROJECT NUMBER</b>		
						<b>5e. TASK NUMBER</b>		
						<b>5f. WORK UNIT NUMBER</b>		
<b>7. PERFORMING ORGANIZATION NAME(S) AND ADDRESS(ES)</b> Department of Aerospace and Mechanical Engineering University of Notre Dame, Notre Dame, IN 46556						<b>8. PERFORMING ORGANIZATION REPORT NUMBER</b>		
<b>9. SPONSORING/MONITORING AGENCY NAME(S) AND ADDRESS(ES)</b> Air Force Office of Scientific Research  875 N Randolph St, Suite 325, Room 3112  Arlington, VA 22203						<b>10. SPONSORING/MONITORING AGENCY ACRONYM(S)</b> AFOSR		
						<b>11. SPONSORING/MONITORING AGENCY REPORT NUMBER(S)</b>		
						AFRL-OSR-VA-TR-2012-1152		
<b>12. DISTRIBUTION/AVAILABILITY STATEMENT</b> Approved for public release; distribution unlimited.								
<b>13. SUPPLEMENTARY NOTES</b> Report contains color.								
<b>14. ABSTRACT</b> This report presents results of experimental studies of aero-optical effects, both in time-averaged and instantaneous sense, caused by compressible turbulent boundary layers. The results were used to investigate the physical mechanism of aero-optical distortions and to develop various models to predict aero-optical effects for both subsonic and supersonic Mach numbers, laser beam sizes and non-adiabatic walls. The developed models were shown to correctly predict experimentally-observed level of aero-optical distortions. The temperature mismatch between the flow and the wall was systematically studied and modeled and it was shown to have a profound effect on the level aero-optical aberrations. Detailed studies of the beam size on the spatial statistics of aero-optical structures were also carried out in this work. Finally, statistics of the instantaneous far-field drop-outs, like their time-duration, frequency and strength, were investigated and various tools were developed to predict and properly address a potentially-damaging impact from boundary layers on the laser communication airborne systems.								
<b>15. SUBJECT TERMS</b> Aero-optics, free-space communication, boundary layer, modeling								
<b>16. SECURITY CLASSIFICATION OF:</b>			<b>17. LIMITATION OF ABSTRACT:</b>	<b>18. NUMBER OF PAGES</b> 50	<b>19a. NAME OF RESPONSIBLE PERSON (Monitor)</b> Dr. Douglas R. Smith <b>19b. TELEPHONE NUMBER (Include Area Code)</b> (703) 696-6219			
<b>a. REPORT</b> Unclassified	<b>b. ABSTRACT</b> Unclassified	<b>c. THIS PAGE</b> Unclassified						

# **The Physics of Boundary-Layer Aero-Optic Effects**

## **Final Report**

**AFOSR Grant FA9550-09-1-0449**  
**Program manager: Dr. Douglas Smith**

Principal Investigator: Stanislav Gordeyev  
Co-Principal Investigator: Eric J. Jumper  
Department of Aerospace and Mechanical Engineering  
University of Notre Dame, IN 46556  
(574) 631-4338  
E-mail: [sgordeye@nd.edu](mailto:sgordeye@nd.edu)

Period Covered: 1 May 2009 – 31 April 2012

# REPORT DOCUMENTATION PAGE

*Form Approved*  
OMB No. 0704-0188

The public reporting burden for this collection of information is estimated to average 1 hour per response, including the time for reviewing instructions, searching existing data sources, gathering and maintaining the data needed, and completing and reviewing the collection of information. Send comments regarding this burden estimate or any other aspect of this collection of information, including suggestions for reducing this burden, to Department of Defense, Washington Headquarters Services, Directorate for Information Operations and Reports (0704-0188), 1215 Jefferson Davis Highway, Suite 1204, Arlington, VA 22202-4302. Respondents should be aware that notwithstanding any other provision of law, no person shall be subject to any penalty for failing to comply with a collection of information if it does not display a currently valid OMB control number. **PLEASE DO NOT RETURN YOUR FORM TO THE ABOVE ADDRESS.**

<b>1. REPORT DATE (DD-MM-YY)</b> September 2012			<b>2. REPORT TYPE</b> Final			<b>3. DATES COVERED (From - To)</b> 01 May 2009 – 30 April 2012		
<b>4. TITLE AND SUBTITLE</b> The Physics of Boundary-Layer Aero-Optic Effects						<b>5a. CONTRACT NUMBER</b>		
						<b>5b. GRANT NUMBER</b> FA9550-09-1-0449		
						<b>5c. PROGRAM ELEMENT NUMBER</b>		
<b>6. AUTHOR(S)</b> Stanislav Gordeyev and Eric J. Jumper (University of Notre Dame)						<b>5d. PROJECT NUMBER</b>		
						<b>5e. TASK NUMBER</b>		
						<b>5f. WORK UNIT NUMBER</b>		
<b>7. PERFORMING ORGANIZATION NAME(S) AND ADDRESS(ES)</b> Department of Aerospace and Mechanical Engineering University of Notre Dame, Notre Dame, IN 46556						<b>8. PERFORMING ORGANIZATION REPORT NUMBER</b>		
<b>9. SPONSORING/MONITORING AGENCY NAME(S) AND ADDRESS(ES)</b> Air Force Office of Scientific Research  875 N Randolph St, Suite 325, Room 3112  Arlington, VA 22203						<b>10. SPONSORING/MONITORING AGENCY ACRONYM(S)</b> AFOSR		
						<b>11. SPONSORING/MONITORING AGENCY REPORT NUMBER(S)</b>		
<b>12. DISTRIBUTION/AVAILABILITY STATEMENT</b> Approved for public release; distribution unlimited.								
<b>13. SUPPLEMENTARY NOTES</b> Report contains color.								
<b>14. ABSTRACT</b> This report presents results of experimental studies of aero-optical effects, both in time-averaged and instantaneous sense, caused by compressible turbulent boundary layers. The results were used to investigate the physical mechanism of aero-optical distortions and to develop various models to predict aero-optical effects for both subsonic and supersonic Mach numbers, laser beam sizes and non-adiabatic walls. The developed models were shown to correctly predict experimentally-observed level of aero-optical distortions. The temperature mismatch between the flow and the wall was systematically studied and modeled and it was shown to have a profound effect on the level aero-optical aberrations. Detailed studies of the beam size on the spatial statistics of aero-optical structures were also carried out in this work. Finally, statistics of the instantaneous far-field drop-outs, like their time-duration, frequency and strength, were investigated and various tools were developed to predict and properly address a potentially-damaging impact from boundary layers on the laser communication airborne systems.								
<b>15. SUBJECT TERMS</b> Aero-optics, free-space communication, boundary layer, modeling								
<b>16. SECURITY CLASSIFICATION OF:</b>			<b>17. LIMITATION OF ABSTRACT:</b>	<b>18. NUMBER OF PAGES</b> 50	<b>19a. NAME OF RESPONSIBLE PERSON (Monitor)</b> Dr. Douglas R. Smith <b>19b. TELEPHONE NUMBER (Include Area Code)</b> (703) 696-6219			
<b>a. REPORT</b> Unclassified	<b>b. ABSTRACT</b> Unclassified	<b>c. THIS PAGE</b> Unclassified						

Standard Form 298 (Rev. 8-98)  
Prescribed by ANSI Std. Z39-18

## Table of Contents

Section	Page
REPORT DOCUMENTATION PAGE.....	ii
Table of Contents .....	iii
1. Summary .....	1
2. Introduction .....	2
2.1 Background .....	2
2.2 Research Goals.....	6
3. Experimental Set-Up.....	6
3.1 Subsonic Facilities .....	6
3.2 Supersonic Facilities .....	8
3.3 2-D Wavefront Data Collection .....	9
3.4 1-D Wavefront Collection Using Malley Probe.....	10
3.5 Streamwise Variation in BL Statistics .....	11
4. Results and Discussion.....	12
4.1 Optical Data Reduction and Analysis .....	12
4.1.1 Malley Probe 1-D Wavefront Data Reduction.....	12
4.1.2 Relation Between Deflection-Angle Spectra and Wavefront Statistics.....	13
4.1.3 Shack-Hartman Wavefront Sensor Data Reduction.....	15
4.1.4 Spectral Analysis of Wavefronts.....	16
4.2 Models of Optical Distortions.....	18
4.2.1 Aero-Optical Model for Subsonic Boundary Layer with Non-Adiabatic Wall ..18	
4.2.2 Model for Aero-Optical Distortions for Compressible Boundary Layers .....	25
4.3 Finite Aperture Affects .....	28
4.4 Optical Corellation Results .....	30
4.4.1 Streamwise Correlation Length.....	30
4.4.2. Spanwise Correlation .....	32
4.5 Instantaneous Far-Field Intensity Drop-Outs.....	32
4.5.1 Absolute SR threshold .....	36
4.5.2 Relative intensity variation .....	39
5. Conclusions and Discussion.....	40
6. References .....	43
Appendix .....	46
List of Publications Based in Whole or in Part on Results from the Current Program ...	46

## **Acknowledgements**

The authors thank the Director for Aeronautics Research Center, USAFA, Dr. Thomas McLaughlin for providing the opportunity to conduct optical measurements in Trisonic Tunnel at the Air Force Academy.

This work was supported by AFOSR, Grant FA9550-09-1-0449. The U.S. Government is authorized to reproduce and distribute reprints for government purposes notwithstanding any copyright notation thereon.

## 1. Summary

It has always been assumed that using a conformal window as the exit pupil for an airborne laser avoids aero-optic environments that cause the laser to break up in the far field; however, it was recently discovered that while the average intensity on the target is relatively large, projection through turbulent boundary layers causes short dropouts to very low intensity. Such dropouts are particularly damaging to laser-transmitted Free-Space Communication. The objective of this program is to understand the physics of the aero-optic environment created by high-subsonic turbulent boundary layers in order to develop predictive models for these effects and to discover mitigation strategies.

Although the program pursued fundamental studies of turbulent boundary layers, it also has a relevance to specific Air Force and DoD applications, such as potentially damaging and deteriorating effects aero-optical distortions caused boundary layers have on laser-based communication systems using conformal windows with large apertures and phased-laser arrays.

This program represents the first systematic effort to bring together all that is now known about the optical character of attached turbulent boundary layers and to systematically study the specific character of the structures within the boundary layer that are responsible for the dropouts already seen in some of our earlier work. These studies include adiabatic, heated and cooled walls.

This report presents results of extensive and carefully-designed experimental studies of aero-optical effects, both in time-averaged and instantaneous sense, caused by compressible turbulent boundary layers. The results were used to investigate the physical mechanism of aero-optical distortions and to develop various models to predict aero-optical effects for both subsonic and supersonic Mach numbers, laser beam sizes and non-adiabatic walls. The developed models were shown to correctly predict experimentally-observed level of aero-optical distortions. An adiabatic cooling/heating (the Extended Strong Reynolds Analogy) was identified as the main mechanism causing the density fluctuations and related aero-optical distortions inside boundary layers. The temperature mismatch between the flow and the wall was systematically studied and modeled and it was shown to have a profound effect on the level aero-optical aberrations, as the heated wall amplifies them and the cooled wall significantly reduces distortions. This never-before-observed cooled-wall effect provides an efficient passive way to mitigate aero-optical distortions. Detailed studies of the beam size on the spatial statistics of aero-optical structures were also carried out in this work. Finally, statistics of the instantaneous far-field drop-outs, like their time-duration, frequency and strength, were investigated and various tools were developed to predict and properly address a potentially-damaging impact from boundary layers on the laser communication airborne systems.

All these studies become possible largely due to the development of a suite of sufficiently sensitive and high-bandwidth wavefront sensors and data reduction techniques to capture instantaneous information necessary to understand the cause of these optical distortions.

## 2. Introduction

### 2.1 Background

When a collimated laser beam propagates through a turbulent compressible flow, different parts of its wavefront travel at different speeds and the wavefront becomes aberrated, as the local speed of light,  $u$ , is a function of the local index-of-refraction,  $n$ ,  $u/c = 1/n$ , where  $c$  is the speed of light in a vacuum. The index-of refraction in turn depends on the media density,  $\rho$ , via a Gladstone-Dale relation, [1],  $\rho = K_{GD}(n-1) = K_{GD}n'$ , where  $K_{GD}$  is a Gladstone-Dale constant. This constant depends on the gas mixture and the laser wavelength [2]; for air over the visible wavelength range  $K_{GD}$  is approximately  $2.27 \times 10^{-4} \text{ m}^3/\text{kg}$ .

These optical aberrations caused by either density fluctuations present in the atmosphere, known as the *atmospheric-propagation* problem [3], or inside a relatively-thin region of turbulent flow, comprised of compressible shear layers, wakes and turbulent boundary layers around an airborne platform, known as the *aero-optic* problem [4], can severely degrade the performance of an airborne laser system, be it free-space communication, interrogation, targeting or a direct energy application. The impact of these degrading effects can be quantified in different ways; however one of the most common is to quantify it in terms of a time-averaged Strehl ratio,  $SR$ , defined as time-averaged ratio of the actual on-axis intensity at the target,  $\bar{I}$ , to the distortion-free, diffraction-limited intensity,  $I_0$ ,  $SR = \bar{I} / I_0$ .

When the propagation length is relatively short, the levels of wavefront distortions can be quantified by Optical-Path-Length,  $OPL(x,y,t)$ ,

$$OPL(x, y, t) = \int_a^b n'(x, y, z, t) dz = K_{GD} \int_a^b \rho'(x, y, z, t) dz$$

where the integration is performed along the beam propagation axis,  $z$ , and spatial distributions are given on a  $(x,y)$ -plane normal to the  $z$ -axis. A spatially-averaged mean is commonly subtracted from  $OPL$  and defined as Optical-Path-Difference,

$$OPD(x, y, t) = OPL(x, y, t) - \langle OPL(x, y, t) \rangle,$$

where brackets denote the spatial averaging in the  $(x,y)$ -plane. Typically, the spatial root-mean-square of  $OPD$  at each instant in time,  $OPD_{\text{rms}}(t)$ , and the time-averaged spatial root-mean-square of  $OPD$ ,  $OPD_{\text{rms}}$ , are computed.

In recent years most of the work in aero-optics has been on the aberrating effects of separated shear layers, as they have been shown to be the most aero-optically-distorting flows; however, the first work in aero-optics was actually for turbulent boundary layers [5]. The first theoretical study was done by Liepmann [6] and published as a Douglas Aircraft Company Technical Report and made use of the jitter angle of a thin beam of light as it traveled through the compressible boundary layer on the sides of high-speed wind tunnels as a way to quantify the crispness of Schlieren photographs. A significant piece of work was done in 1956 by Stine and Winovich [7]; they performed photometric measurements of the time-averaged radiation field at the focal plane of a receiving telescope in an attempt to validate Liepmann's formulations. Their work brought together all that had been done till then on optical propagation through index-variant turbulent flows. Their work also raised the prospect of using an optical degradation measurement as a method of inferring turbulence scales. Based heavily on the approach taken by Tatarski [3] for electromagnetic waves propagated through the atmosphere, in the early 1960's Sutton produced the most-widely referred to theoretical formulation for the aberrating effects of

turbulent boundary layers based on statistical measures of the turbulence [6] and developed a “linking equation” between the turbulence quantities and the optical distortions [8],

$$OPD_{rms}^2 = 2K_{GD}^2 \int_0^L \rho_{rms}^2(y) \Lambda_y(y) dy \quad (1)$$

where  $\rho_{rms}(y)$  is the density fluctuations along the beam direction and  $\Lambda_y(y)$  is a density correlation length. The equation (1) assumes that the density covariance can be approximated by the exponential form and if the covariance is approximated by the Gaussian function, the pre-multiplier in Equation (1) should be replaced with  $\sqrt{\pi}$  [9]. In our analysis we used the value of 2 for the pre-multiplier.

Interestingly, by incorporating the realization first reported by Malley, et. al. [10] that aberrations produced by a laser propagated through convecting flow structures themselves convect, it can be shown that both Liepmann’s and Sutton’s formulations are identical [5]. Due to the same motivation that produced Eq. (1), work on the turbulent boundary layer intensified in the late 1960’s and through the decade of the 1970’s due to an interest in placing lasers on aircraft. In the 1970’s Rose [11] conducted the most extensive, at that time, experimental studies of optical aberrations caused by a turbulent boundary layer. He conducted hot-wire measurements in turbulent boundary layers in order to indirectly obtain their density fluctuations,  $\rho'(y)$ , (assuming that pressure fluctuations inside the boundary layer were zero) and associated correlation lengths,  $\Lambda_\rho(y)$ . These were used to estimate wavefront aberrations that would be imprinted on a laser beam propagated through the same turbulent boundary layer assuming homogeneous turbulence. The on-average wavefront aberrations, in the form of  $OPD_{rms}$ , were estimated using Sutton’s linking equation (1). Rose empirically found  $OPD_{rms}$  to be *proportional* to dynamic pressure,  $q$ , and boundary layer thickness,  $\delta$ , such that  $OPD_{rms} \sim q \delta$ .

These aircraft hot-wire measurements were complemented by the work of Gilbert [12], who performed interferometer measurements. In the Gilbert work, the interferometry used a double-pulse technique, which measured the difference in the wavefront from one pulse to another, rather than the distorted wavefront at a given instant, and only a limited number of these were made. Gilbert reported that the interferometry *generally* supported the hot-wire, integral-method estimations of the  $OPD_{rms}$ ; however, based on his work Gilbert concluded that the *square* of the  $OPD_{rms}$  depended *linearly* on the dynamic pressure,  $OPD_{rms}^2 \sim q$ .

A review of the major publication in aero-optics [4] from the 1970’s demonstrates that work up until 1982 focused on the measurement of the time-averaged, spatial, near-field optical distortion,  $OPD_{rms}$ , either by direct optically-based methods, or assessed indirectly using fluid-mechanic measurements via the linking equation (1). Optical methods of that time that have been applied to the measurement of the near-field time-averaged phase variance include direct interferometry, pulsed interferometry, and shearing interferometry. These interferometric methods provided a time-averaged assessment of the optical phase variance over the aperture; however, these methods provided no information concerning temporal frequencies.

In 1994, Masson et. al. [13] revisited the Gilbert and Rose data and concluded that after removing systematic errors from Gilbert’s data,  $OPD_{rms} \sim (\rho M^2)^{1.16}$ . Also he found that there appeared to be a systematic difference between direct and indirect wavefront error measurements, with the interferometric estimates consistently yielding higher estimates of the  $OPD_{rms}$  than the hot-wire estimates, but could not offer a reasonable explanation why optical and hot-wire data did not agree in magnitude. The appearance of Masson’s 1994 paper revisiting data taken through the early 1980’s is evidence that interest/funding in aero-optics had long come to

an end. In fact, in a 1985 paper Sutton [14] announced that aero-optics was a mature discipline requiring only the measurement of the turbulence statistics of a few additional flows.

In 1990s these arguments were revisited based on the fact that newer lasers envisioned for airborne platforms were an order of magnitude shorter wavelength than those of the 1970's and 1980's. In the 1970's and 1980's the airborne laser system of the day was the Airborne Laser Laboratory, ALL, which used a CO<sub>2</sub> laser with a wavelength of 10.6 μm. The typical level of optical aberrations by the boundary layer is  $OPD_{rms} \sim 0.1 \mu\text{m}$  and, at this wavelength it would reduce the Strehl ratio by less than 1%. This estimation is based on the large aperture approximation [15] for the fraction of diffraction-limited intensity on target based on the  $OPD_{rms}$  and laser wavelength,  $\lambda$ , as

$$\overline{SR} \approx \exp \left[ - \left( \frac{2\pi OPD_{rms}}{\lambda} \right)^2 \right]$$

Notice that the exponent scales as  $(1/\lambda)^2$ ; today, wavelengths of interest are in the near-IR ( $\sim 1 \mu\text{m}$ ) and visible. Thus, the  $OPD_{rms}$  predicted by Gilbert and Rose ( $\sim 0.1 \mu\text{m}$ ) that were known to be inconsequential at the wavelength of 10.6 μm now drop the Strehl ratio by about 30% or even more; as such, there is now a renewed interest in revisiting the turbulent-boundary-layer problem.

Also, there now exist direct optical instrumentation capable of assessing not only the  $OPD_{rms}$ , but also the spatial and temporal frequencies of the aberrations, and, as will be described below, the ability to construct wavefronts from which the far-field intensity pattern can be computed directly. Using the time-resolved time series of far field patterns, Strehl ratio as a function of time can be computed. From the point of view of applications to free-space communication, which are concerned with bit error rate, these time series of instantaneous Strehl ratio are more instructive than their average; however, once the time series are available the time-averaged Strehl ratio can be computed, which is of interest to directed energy applications that depend only on maintaining an average intensity above some critical threshold.

Finally, because conformal windows, which presume an attached turbulent boundary layer, as opposed to beam-directing turrets, which require beam propagation through regions of separated flow, are now being considered for exit pupils, it is critical that a more reliable method of predicting the turbulent-boundary-layer's aberration character for various flight conditions is needed. In addition, with the new ability to obtain direct, high-fidelity optical data without resorting to indirect methods of predicting the optical aberrations, it is now more efficient to revisit the question of scaling of the aero-optic data.

The pioneering use of a new wavefront device called a Malley probe in making optical measurements in turbulent subsonic boundary layers [16] has shown to give the most accurate and highly time-resolved information about optical distortions with bandwidths  $> 100 \text{ kHz}$ . It was found [16, 17] that optical distortions were proportional to the boundary layer thickness, the freestream density and the square of the freestream Mach number,  $OPD_{rms} \sim \delta \rho M^2$ , which is consistent with the finding by Rose [11], but not with Gilbert [12] or Masson [13]. It was also found that optical distortions convect at speeds of 0.82-0.85 of the freestream speed, which suggest that optically-active structures reside in the outer portion of the boundary layer.

To our knowledge the only other experimental investigations of optical distortions caused by turbulent boundary layers since the work of the 1980's and 1990's was the study at Princeton [18]. That study made use of a high-speed camera to make a high-bandwidth Shack Hartmann Sensor and then applied it to the investigation of transonic and supersonic boundary layers with

and without surface injection of various gases. Unfortunately the signal-to-noise ratio of the sensor introduced much uncertainty into their results and conclusions drawn from them. Regardless of the uncertainty in their results, they proposed a scaling law that was based on a model that presumed that the pressure fluctuations in the boundary layer are negligible, invoking the “Strong Reynolds Analogy,” [19].

Because of great challenges in accurately computing a time-resolved, compressible boundary layer at high transonic Mach numbers, only few attempts to numerically compute optical aberrations inside turbulent boundary layers have been made. Truman and Lee [20] and Truman [21] used a DNS spectral method to calculate time-dependent optical distortions for a low-Reynolds-number boundary layer, where the density fluctuations were computed temperature fluctuations due to temperature being transported as a passive scalar under the assumption of constant pressure. Large-scale streamwise elongated regions of highly-correlated optical distortions were found and the link between highly anisotropic hairpin vortical structures leading to the optical distortions were observed. Also it was found that the optical distortions were anisotropic and vary significantly with the propagation (elevation) angle. Tromeur et al. [22-24] calculated optical aberrations by a compressible turbulent boundary layer at subsonic ( $M = 0.9$ ) and supersonic ( $M = 2.3$ ) speeds for  $Re_\theta = 2917$  using large-eddy simulations, LES, which compared favourably with some limited experimental data [25]. They found that the optical aberrations traveled at 0.8 of the freestream speed and were dominated by large-scale structures residing in the outer portion of the boundary layer.

The purpose of this report is to present the results of comprehensive experimental studies of the aero-optical effects caused by subsonic and supersonic turbulent boundary layers over a range of boundary-layer thicknesses, freestream Mach numbers, aperture sizes and non-adiabatic walls. Although our first meeting paper on the optical character of high-subsonic turbulent boundary layers was in 2003 [16], it has taken these many years to assure ourselves that the data included in this report and conclusions drawn from them will not change appreciably with the continued advance in instruments and techniques. As mentioned previously, these early conclusions are heavily dependent on the use of the Malley Probe; however, in the present work much effort has been made to make direct comparison of the Malley Probe results with other wavefront instruments used to interrogate the same flows. Further, accurate and repeatable data required the development of techniques for increasing signal-to-noise ratios and methods of removing corrupting influences as well as understanding the effect of aperture size on suppression or proper filtering of the data.

As the results in this program depend on the instruments used, Section 3 describes experimental-set-ups used and the optical sensors used to collect optical data, the Malley probe, which is capable of accurately measuring small levels of optical aberrations and their average convective speeds and the high-speed Shack-Hartmann Sensor. Section 4 presents and discusses the results of the optical measurements, including detailed description of the data reduction procedures for both sensors in Section 4.2. Section 4.3 presents models to predict aero-optical distortions for compressible supersonic boundary layers and for non-adiabatic walls; both models are shown to provide correct scaling laws for the experimentally-observed results. Sections 4.4 and 4.5 discuss finite-beam-size aperture effects on the level of the aero-optical distortions and correlation lengths. Section 4.6 presents a detailed investigation of statistics of the far-field intensity drop-outs and provides important applied tools to estimate aero-optical impact on airborne laser communication systems. A summary of conclusions and additional discussion of the results are given in Section 5.

## 2.2 Research Goals

The main goal of the program was a coherent fundamental study of the structure of turbulence in compressible boundary layers, in particular, its density structure in order to identify a physical mechanism of aero-optical distortions caused by compressible turbulent boundary layers. Specifically, the program was designed to achieve the following tasks:

1. Develop wavefront-sensing instrumentation and techniques to accurately measure spatially- and temporally-resolved wavefronts.
2. Study the role of pressure fluctuations as an additional source of aero-optical distortions.
3. To develop useful scaling laws and models to predict aero-optical effects caused by turbulent boundary layers at different subsonic and supersonic regimes and boundary layer conditions and investigate “real-life” effects, such as non-adiabatic, that is heated or cooled wall-temperature effects.
4. Study the impact of boundary-layer-related aero-optical distortions on the performance of airborne laser communication systems, with the emphasis in aero-optically-related intensity drop-outs on the target.
5. Study the effect of different aperture sizes on the level of aero-optical distortions and related correlation lengths.

## 3. Experimental Set-Up

### 3.1 Subsonic Facilities

Experimental aero-optical measurements of the subsonic turbulent boundary layer were conducted at the Mach 0.6 closed-loop wind tunnel at the Hessert Laboratory for Aerospace Research - White Field at the University of Notre Dame, shown in Figure 1. The test section has a square cross section with sides of 91.4 cm and a length of 2.75 m. For all wavefront measurements, optical-quality glass windows were installed in the test section wall to ensure accurate optical measurements of the boundary layer.

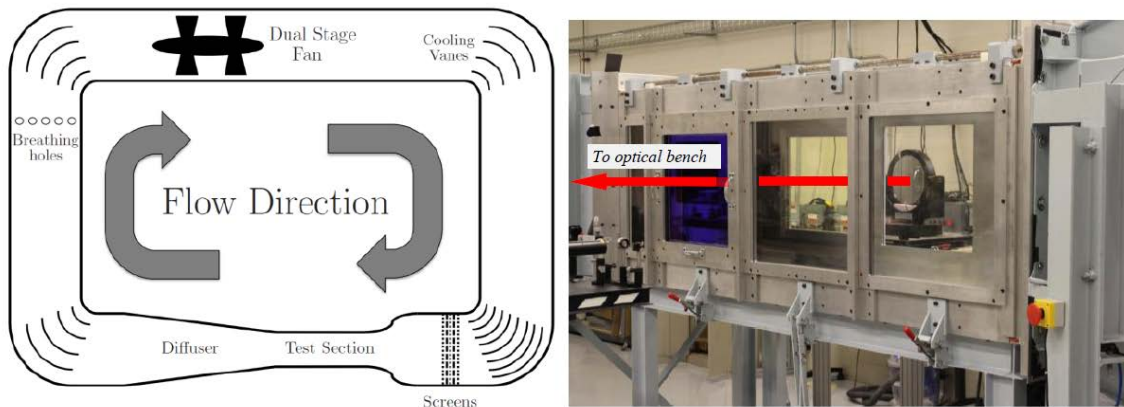


**Figure 1. Schematic of the Mach 0.6 closed-loop wind tunnel taken from Cress [26], (left), and a photo of the test section configured for boundary layer wavefront measurements.**

Aero-optical measurements were collected through a turbulent boundary layer at two streamwise locations in this wind tunnel, at approximately 1.50 m and 2.00 m from the start of the test section. Boundary layer thickness values at these locations were reported to be

approximately 3.2 cm and 3.7 cm respectively based on data from earlier characterizations of the boundary layer in this facility [26].

An additional set of measurements were taken in a Transonic Wind Tunnel at the Hessert Laboratory for Aerospace Research at the University of Notre Dame. The wind tunnel, shown in Figure 2, has an open circuit configuration with a 150:1 contraction ratio. Velocity is varied by controlling the pressure in the plenum, which is located just downstream of the diffuser section. The boundary layer test section has a cross section measuring 9.9 cm by 10.1 cm, with a development length of 155 cm from the contraction to the measurement station. During experiments, the freestream velocity was monitored directly using a Pitot-static probe. The boundary layer displacement thickness,  $\delta^*$ , was 3.6 mm and the momentum thickness,  $\Theta$ , was found to be 2.75 mm. The Reynolds number based on the momentum thickness,  $Re_\Theta = U_\infty \Theta / \nu$ , was approximately 35,400 at this station and the Reynolds number based on the development length  $x = 170$  cm,  $Re_x = U_\infty x / \nu$ , was approximately  $21.9 \times 10^6$ . The shape factor  $H = \delta^* / \Theta$  for this boundary layer was 1.3, which agrees well with values for zero-pressure-gradient boundary layers [27] at this  $Re_\Theta$ .

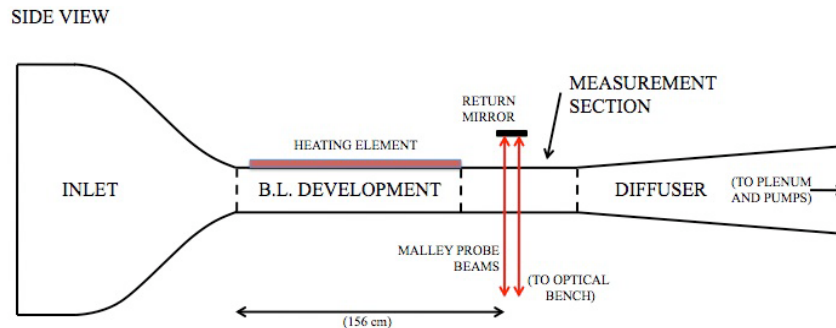


**Figure 2. Schematic of the Hessert Laboratory transonic wind tunnel, from [26].**

For non-adiabatic wall experiments, one wall of the boundary layer development section was replaced with an aluminum plate. To create a heated boundary layer, flexible, electric resistive coil heaters were epoxied to the outside surface of the aluminum plate and insulated, see Figure 2. The temperature of the heaters were controlled with a PID circuit with the temperature input coming from a thermal tab embedded flush to the inside wall which measured the wall surface temperature. The thickness of the aluminum plate was 5 mm to ensure a uniform wall surface temperature. Several wall temperatures were tested at each Mach number; it should be noted that due to the fixed output power of the electric heaters, the maximum achievable wall temperature was dependent on the flow speed, with a greater difference between the freestream and the wall temperature achieved in the transonic tunnel at Mach 0.2 ( $\Delta T \sim 28^\circ\text{C}$ ) than at Mach 0.6 ( $\Delta T \sim 15^\circ\text{C}$ ). Due to the differences in the low speed tunnel size and the slightly different configuration of the heating elements, the maximum temperature difference in the low speed tunnel was  $10^\circ\text{C}$ .

To create a cooled boundary layer, the heating elements were removed from the aluminum plate along the length of the development section; the thermal tab remained embedded on the inside wall to measure the wall temperature beneath the boundary layer. A mixture of snow, ice and water was used to cool the wall prior to beginning airflow in the tunnel. Three Mach numbers were tested: 0.3, 0.4, and 0.5 and different temperature differences were

achieved at each Mach numbers, with the greatest difference,  $\Delta T \sim -12^\circ\text{C}$ , at Mach 0.3 and  $\Delta T \sim -4^\circ\text{C}$  at Mach 0.5.

### 3.2 Supersonic Facilities

All supersonic aero-optical measurements were performed in the Trisonic Wind Tunnel at the US Air Force Academy in Colorado Springs. The tunnel is an open circuit, blow-down-type facility, with a range of Mach numbers between 0.24 - 4.5. The tunnel is shown schematically in Figure 3, top. Air is passed through several stages of filters and dryers, and is compressed by two rotary screw compressors, 260 kW each to six 25-m<sup>3</sup> storage tanks at pressures up to 40 atmospheres. The stored air is heated to approximately 38 C to prevent complications due to water condensation and ice formation during high-Mach-number tests. The tunnel has a 0.3 m x 0.3 m cross-section test section with two 0.3-meter round optical windows on both sides of the test section, see Figure 3, bottom.

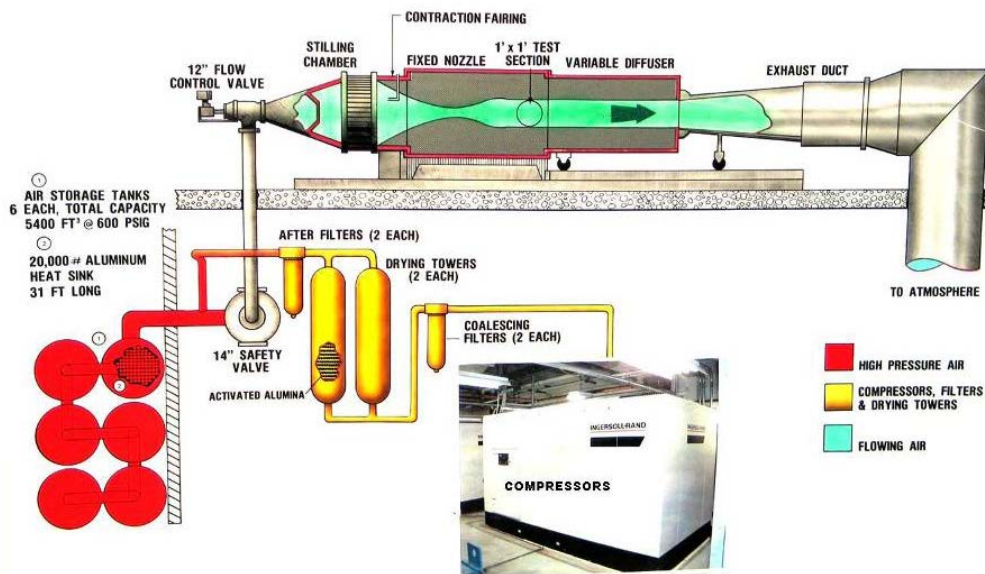


**Figure 3. Top: Schematic of the US Air Force Academy Trisonic Wind Tunnel. Bottom: The test section with 0.3-meter-diameter optical windows.**

For all tests the freestream Mach number was 2.0; to change the test section static density the plenum pressure was varied between 3.4 and 6.8 atmospheres, so the test section static

pressure was varied between 0.4 and 0.8 atmospheres. The results presented in this report were obtained with a plenum pressure of 5.4 atmospheres. The static temperature was estimated to be between -107 C and -109 C for different runs using the total temperature measurements and the isentropic relation.

### 3.3 2-D Wavefront Data Collection

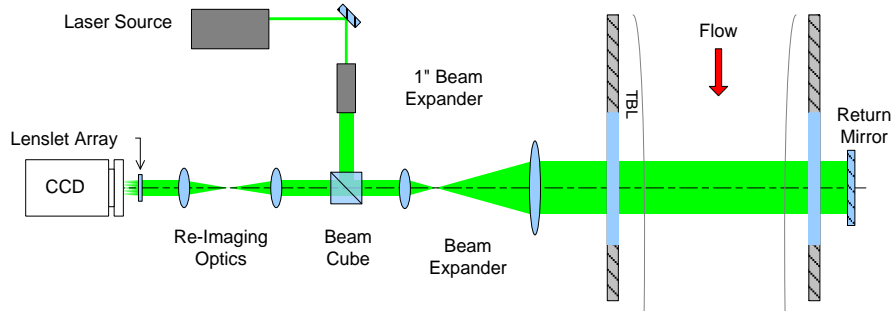


**Figure 4. Schematic of the double-pass boundary layer measurements for the Shack-Hartmann wavefront sensor.**

Spatially- and temporally-resolved boundary-layer wavefront measurements were acquired using a high-speed Shack-Hartmann wavefront sensor. Aero-optical wind tunnel measurements were made using a double-pass boundary layer method, with a basic optical set-up shown in Figure 4. Under the assumption that the two boundary layers are statistically independent, the resulting time-averaged ‘optical energy’,  $OPD_{rms}^2$ , is a sum of individual ‘optical energies’ from each boundary layer. Therefore, the optical aberration from the single boundary layer can be estimated from the double boundary layer measurements as  $OPD_{rms}^{SBL} = \frac{1}{\sqrt{2}} OPD_{rms}^{DBL}$ , where SBL and DBL stands for the single and double boundary-layer experiments. As it was shown in [17], this approach is fully vindicated by comparing the double-boundary-layer results with the single-boundary-layer results.

Several magnifications for the beam expander, shown as part of the wavefront sensor in Figure 4, were also used to study the effects of aperture diameter on various wavefront statistical quantities. Samples were acquired for different combinations of sampling frequency, spatial resolution, and the aperture size. The test matrix for data is shown in the Table 1.

**TABLE 1: WAVEFRONT DATA ACQUISITION PARAMETERS.**

Facility	$\delta$ [cm]	$Ap$ [cm]	$f_{samp}$ [kHz]	Lenslet Resolution
White Field	3.7	2.54	9.5	$60 \times 60$
"	"	5.08	9.5	$60 \times 60$
"	"	10.2	9.5	$60 \times 60$
"	"	10.2	25	$30 \times 30$
Hessert	2.4	5.08	50	$30 \times 15$
"	"	10.8	50	$30 \times 15$

It should be noted that the historic issue with digital-camera-based wavefront sensors has been a tradeoff between spatial resolution and frequency resolution. Acquisition parameters,

shown in Table 1, clearly demonstrates that although significant advances in the frequency response of wavefront sensor CCDs have been made, achieving frequency response on the order of 50 kHz requires a reduction in spatial resolution. For aero-optically active flows which are spanwise homogeneous such as the turbulent boundary layer this is a trade which is easily made.

### 3.4 1-D Wavefront Collection Using Malley Probe

Additional wavefront measurements of the subsonic and supersonic boundary layers were acquired using the Malley Probe. The device essentially replicates a single lenslet element of a Shack Hartman wavefront sensor using a small-diameter, order of a millimeter, beam. Two or more of these beams may be placed in various arrangements, but typically aligned in the direction of flow, to provide direct measurements of some basic statistics such as levels of aero-optical distortions, the convective velocity and the correlation length, and, in inhomogeneous flows, some estimates of spatial distribution of  $OPD_{rms}$ . The principle of the Malley Probe is described in detail by Gordeyev, et al. [17], and a basic schematic is shown in Figure 5. The laser beam, after passing through the spatial filter, was re-collimated and split into two small, about a millimeter in diameter, parallel beams, separated in the streamwise direction by a known distance. The beam separation was varied between 6 and 11 mm for different runs. The beams were then forwarded into the test section normal to the optical window. The return mirror on the other side of the test section reflected beams back to the optical bench along the same optical path. The returning beams were split off using a cube beam splitter and each beam was focused onto a Position Sensing Device (PSD), capable of measuring instantaneous beam deflections. The sampling frequency for subsonic boundary layer was 100 kHz and 200 kHz for the supersonic boundary layer, the typical sampling time was 15 seconds for wavefront measurements.

One benefit of using the Malley Probe sensor is that the output is an analog signal, which is potentially useful for wavefront measurements in an adaptive optics system or as diagnostic design tool. Additionally, the Malley probe is capable of sampling frequencies up to 500 kHz, far exceeding the threshold of 50 kHz reached with the Shack-Hartmann WF sensor, thus providing excellent temporal resolution. Additionally, the Malley Probe cost compared to a Shack-Hartman sensor is very low, making the Malley Probe an inexpensive aero-optical sensor.

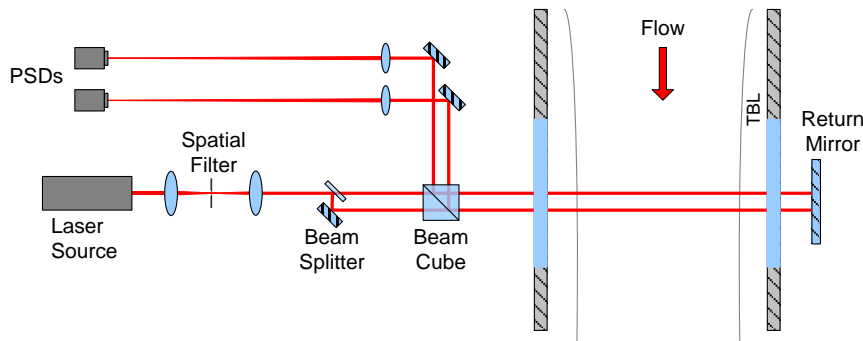


**Figure 5. Schematic of Malley Probe for double-pass boundary layer one-dimensional wavefront measurements.**

However, a main limitation of the Malley Probe as a wavefront sensor is that the output is a single-spatial-point measurement. This limits its ability to provide detailed information about

the instantaneous spatial distribution of aero-optical distortions, which would be readily attainable with a Shack Hartman sensor. Most of the time, the spatial information can be restored assuming that structures simply convect downstream and trade time information for spatial information. Clearly, any information which can be extracted using this method is limited by the extent to which Taylor's Frozen Flow hypothesis holds; for instance the Malley probe cannot properly measure stationary or spatially-evolving aero-optical structures [28]. Finally, the Malley Probe is also susceptible to low-frequency contamination from mechanical vibration of optical components, strong acoustic waves, and signal noise from electronic sources. Additional jitter introduced from these sources becomes nearly indistinguishable from aero-optical contributions in the effected frequency ranges, corrupting the information, although recently several techniques were proposed to in attempt to eliminate vibration-related contaminating issues [29].

### 3.5 Streamwise Variation in BL Statistics

As mentioned before, to analyze measurements collected with the Malley Probe, it is assumed that the streamwise direction is a homogeneous one and time is traded for streamwise coordinate using the Frozen Field assumption [17]. On the other hand, 2-D wavefront data are directly collected over various aperture sizes and, while for small beam apertures, the boundary layer growth is negligible within the aperture, it might become an issue for large apertures. To estimate this effect, one can recall that for the zero-pressure gradient turbulent boundary layer on a flat plate, the boundary layer thickness  $\delta$  can be approximated as  $\delta/x = 0.37 \text{Re}_x^{-1/5}$  via Prandtl's 1/7<sup>th</sup> power law [30]. Writing this relationship in terms of Reynolds number based on the boundary layer thickness, we find that  $\text{Re}_\delta = 0.37 \text{Re}_x^{4/5}$ .

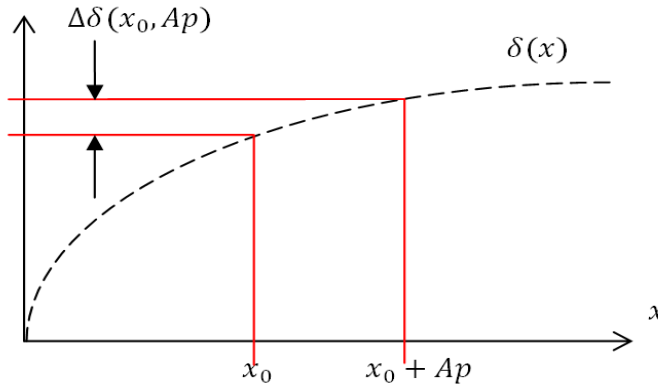


**Figure 6. Schematic showing boundary layer thickness growth over an optical aperture.**

Over an aperture of size  $Ap$ , the boundary layer thickness changes over the aperture by some amount  $\Delta\delta$ , schematically shown in Figure 6, which is proportional to  $\text{Re}_{x+Ap}^{4/5} - \text{Re}_x^{4/5}$ . The ratio of change in the boundary-layer thickness over the aperture to the thickness at the beginning of the aperture then may be expressed as

$$\frac{\Delta\delta(\text{Re}_{Ap})}{\delta} = \frac{0.37(\text{Re}_{x+Ap}^{4/5} - \text{Re}_x^{4/5})}{\text{Re}_\delta} = \frac{\text{Re}_{x+Ap}^{4/5} - \text{Re}_x^{4/5}}{\text{Re}_x^{4/5}},$$

and, since  $\text{Re}_{x+Ap} = \text{Re}_x + \text{Re}_{Ap}$ ,

$$\frac{\Delta\delta(\text{Re}_{Ap})}{\delta} = \left( \frac{\text{Re}_x + \text{Re}_{Ap}}{\text{Re}_x} \right)^{4/5} - 1 = \left( 1 + \frac{\text{Re}_{Ap}}{\text{Re}_x} \right)^{4/5} - 1.$$

Substituting from the equation  $Re_\delta = 0.37 Re_x^{4/5}$  for  $Re_x$ , and expanding the series we finally find that

$$\frac{\Delta\delta(Re_{Ap})}{\delta} = \left(1 + \frac{Re_{Ap}}{3.47 Re_\delta^{5/4}}\right)^{4/5} - 1 = 0.23 \frac{Re_{Ap}}{Re_\delta^{5/4}} + H.O.T..$$

If the first term in this expansion as small,  $0.23Re_{Ap}/(Re_\delta^{5/4}) \ll 1$ , then the variation in the boundary layer thickness over the aperture is negligible. For reported experiments, the maximum aperture was  $Ap = 10.2$  cm and minimum  $Re_\delta$  was  $Re_\delta = 2.2 \times 10^5$ , and the corresponding change in  $\delta$  over the aperture was found to be approximately 4%. So, we can neglect the streamwise variation of the boundary layer thickness and related statistics over the aperture and assume that the streamwise direction is homogeneous over the length of the apertures in this study.

## 4. Results and Discussion

### 4.1 Optical Data Reduction and Analysis

#### 4.1.1 Malley Probe 1-D Wavefront Data Reduction

For the Malley probe, data were acquired as time series of the streamwise beam deflection angle,  $\theta(t)$ , using the analog PSDs and the mean value of the deflection angle for each beam was removed. If a significant amount of low-frequency vibration from various sources is present in the experimental setup, then data can then be high-pass filtered to remove these effects. The time series of deflection angles were used to calculate the streamwise *OPD* via the Frozen Flow hypothesis using the equation,

$$OPD_x(x = -U_c t) = \int_0^t \frac{dOPD(\tau)}{dx} \frac{dx}{d\tau} d\tau = -U_c \int_0^t \theta(\tau) d\tau. \quad (2)$$

The resulting continuous one-dimensional wavefront measurements from the Malley probe were divided into blocks with an aperture of length,  $Ap$ . From each block, streamwise tilt and piston components were removed, and the spatial root-mean-squared value of the wavefront,  $OPD_{rms}$ , was computed as a function of the artificial aperture. Finally,  $OPD_{rms}$  were averaged over all blocks to get the ensemble-averaged value of aero-optical distortion at this streamwise location. Deflection angle amplitude spectra,  $\hat{\theta}(f)$ , were also computed for each Malley probe beam, as well as the spectral cross-correlation,  $S(f) = \langle \hat{\theta}_1(f) \hat{\theta}_2^*(f) \rangle$ , between the beams.

An example of the deflection angle spectrum is shown in Figure 7, left plot. The spectrum has a peak around  $St_\delta \sim 1$ , implying that a dominant source of aero-optical distortions is large, order of the boundary layer thickness, structures. The increase of the spectrum at low frequencies,  $St_\delta < 0.1$ , is due to contamination from mechanical vibration of optical components in the experiment. Sharp peaks at the high-end of the spectrum are related to electronic noise. By cross-correlating beams, the convective velocity can be experimentally calculated from the argument, or the phase of the cross-correlation [17]. The typical phase plot is presented in Figure 7, right plot, showing a linear frequency dependence of the phase over a large frequency domain. Knowing the phase slope, the convective speed can be calculated as  $U_c = \Delta/\tau$  for two beams separated by some distance  $\Delta$ , where  $\tau$  is computed from the slope of the argument as  $dArg[S(f)]/df = 2\pi\tau$ . The convective speed of the boundary-layer-related aero-optical

structures was found to be 0.82 of the freestream speed for subsonic speeds, in agreement with previous measurements, mentioned in the Introduction.

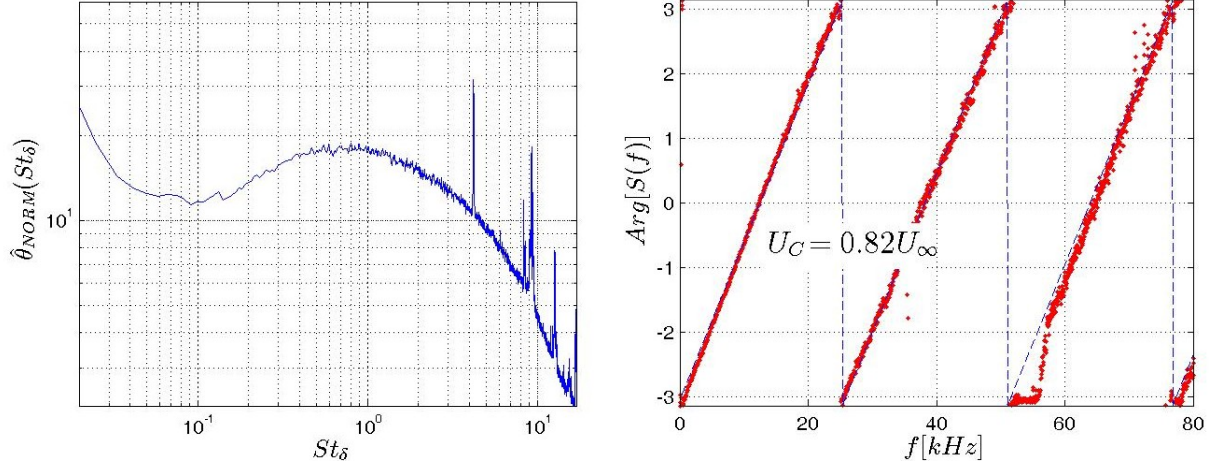


**Figure 7. Typical boundary-layer Malley probe deflection angle amplitude spectrum (left) and the cross-correlation phase plot (right).**

Although the Malley probe measures only 1-dimensional slices of wavefronts, independent 2-dimensional wavefront measurements performed on the same boundary layer using a high-speed Shack-Hartmann sensor [31] and numerical simulations of the turbulent boundary layer [32] confirmed that the Malley probe correctly measures  $OPD_{rms}$ , the correlation lengths and other wavefront statistical properties.

#### 4.1.2 Relation Between Deflection-Angle Spectra and Wavefront Statistics

$OPD$  is a conjugate of the wavefront,  $OPD_{rms}^2 \equiv W_{rms}^2$ . Thus, the  $OPD_{rms}$  is related to the 1-D wavefront power spectrum,  $P_W(k) = \langle \hat{W}(k)\hat{W}^*(k) \rangle$ , as

$$OPD_{rms}^2 \equiv \frac{1}{\pi} \int_0^\infty P_W(k) dk, \quad (3)$$

where  $\hat{W}(k)$  is the Fourier transform of a 1-D wavefront distortion,  $W(x)$ . From Equation (2) it follows that  $\hat{\theta}(f)$  is related to the amplitude spectrum of the wavefront,  $\hat{W}(f)$ ,

$$\hat{W}(f) = U_c \frac{\hat{\theta}(f)}{2\pi f}. \quad (4)$$

So, the wavefront power spectrum can be computed from the deflection angle power spectrum as

$P_W(f) = \left( \frac{U_c}{2\pi f} \right)^2 P_\theta(f)$ . Substituting this equation into (3) and recognizing that  $k = 2\pi f/U_c$ , we get,

$$OPD_{rms}^2 = \frac{1}{\pi} \int_0^\infty P_W(k) dk = \frac{2}{U_c} \int_0^\infty P_W(f) df = \frac{2}{U_c} \int_0^\infty \left( \frac{U_c}{2\pi f} \right)^2 P_\theta(f) df = 2U_c \int_0^\infty \frac{P_\theta(f)}{(2\pi f)^2} df \quad (5)$$

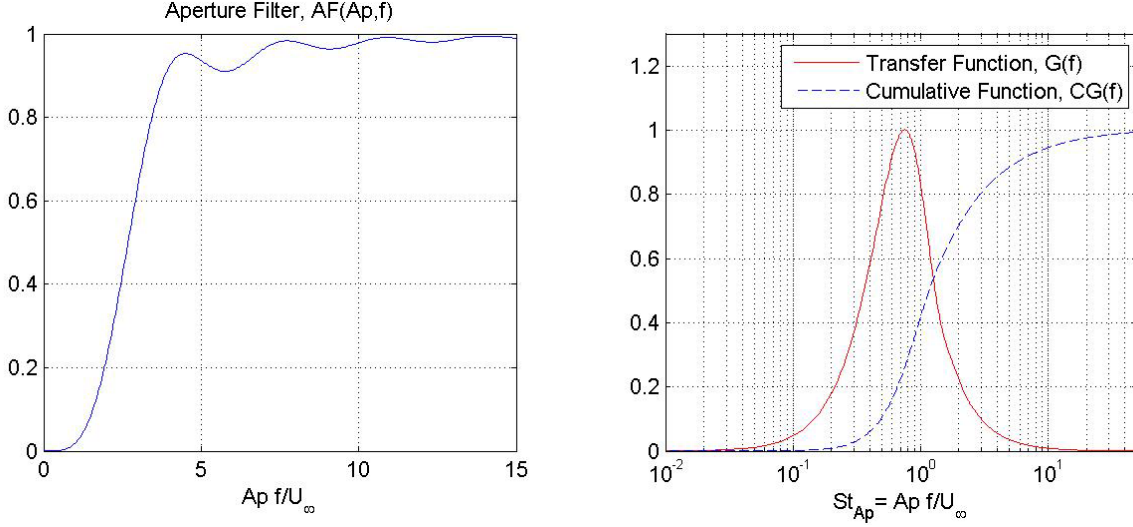


**Figure 8. Left: Aperture filter. Right: Optical transfer and cumulative functions.**

The expression (5) is valid only for an infinite or at least for very large apertures. In [33] it was shown that for finite apertures, the wavefront spectrum should be modified by the inclusion of the wavefront aperture function,  $\hat{W}(f) \rightarrow \hat{W}(f) \cdot AP(Ap, f)$ , where  $AP(Ap, k)$  is a high-pass filter, plotted in Figure 8, left. Thus, the expression for  $OPD_{rms}$ , Eq. (5), should be modified by including the one-dimensional aperture function,  $AF(Ap, f)$ ,

$$OPD_{rms}^2(Ap) = 2U_c \int_0^\infty AF(Ap, f) \frac{P_\theta(f)}{(2\pi f)^2} df = \int_0^\infty G(Ap, f) P_\theta(f) df, \quad (6)$$

where  $G(Ap, f) = \frac{2U_c}{(2\pi f)^2} AF(Ap, f)$  is a transfer function between the deflection angle spectrum and the apertured  $OPD_{rms}(Ap)$ . Figure 8, right, shows the transfer function,  $G(f)$ , normalized by its maximum value as a function of  $St_{Ap} = f Ap / U_\infty$ . The normalized

cumulative transfer function,  $CG(f) = \int_0^f G(x) dx / \int_0^\infty G(x) dx$ , is also plotted in Figure 8, right. The

transfer function is a band-pass filter, centered around  $St_{Ap} = 0.8$ . The low-frequency cut-off is due to aperture effects and the high-frequency cut-off is due to the integral relation between the jitter/deflection-angle signal and the wavefront. Therefore, (6) shows that the measured optical quantity, the jitter/deflection-angle spectrum, should be, in effect, *band-pass filtered* in order to calculate the level of aero-optical aberrations,  $OPD_{rms}$ , for a given aperture size.

From the cumulative function,  $CG(t)$ , see Figure 8, right, it is clear that 95% of the “filtered energy” is located between  $St_{Ap} = 0.28$  and 20. Therefore, the exact shape of the high-pass filter (or more accurately, the fit) which is applied to the measured deflection angles to compensate for vibration contamination is essentially *irrelevant* below  $St_{Ap} = 0.28$  and above  $St_{Ap} = 20$  as long as all non-physical components, like vibrations, are removed or suppressed by the empirical low-pass filter. Direct numerical simulations confirm these results. Detailed discussion of the aperture effects will be presented in Section 4.3.

### 4.1.3 Shack-Hartman Wavefront Sensor Data Reduction

Wavefronts acquired with the high-bandwidth Shack-Hartmann sensor were calculated using commercially-available wavefront processing software. The commercial software calculates wavefronts as a function of aperture coordinate and time. Time-averaged steady lensing and instantaneous tip/tilt and piston modes were removed from the data in post-processing. The spatial root-mean square of OPD was computed at each instant in time in order to obtain the time series  $OPD_{\text{rms}}(t)$  and, finally, the time-averaged  $OPD_{\text{rms}}$  was calculated.

As aero-optical aberrations convect with the flow, it is useful to decompose them into a number of travelling waves. Let us consider one-dimensional ‘slices’ of wavefronts in the streamwise direction and represent them as a sum of a number of travelling modes such that

$$W(x, t) = \sum_{i=0}^N W_i(k_{x_i} x - \omega_i t),$$

From here we can compute the phase velocity of each wave component via the dispersion relation,

$$\omega(k_x) = k_x U_c(k_x), \quad (7)$$

where  $U_c$  is the phase velocity of the travelling wave and in general it is a function of a wavenumber. To find the streamwise convective velocity, temporal evolution of the streamwise ‘slices’ of wavefront data in the middle of the aperture in the spanwise direction,  $W(x, z = \text{fixed}, t)$  were extracted and a normalized wavenumber-frequency amplitude spectra  $\hat{W}_{\text{NORM}}(f, k_x)$  were computed for all experiments,

$$\hat{W}_{\text{NORM}}(f, k_x) = \frac{|\hat{W}(f, k_x)|}{\langle \langle \hat{W}(f, k_x) \rangle \rangle_{k_x} \langle \langle \hat{W}(f, k_x) \rangle \rangle_f}.$$

By looking at the slope of the peak ‘branches’ in this normalized spectrum, convective velocity can be computed through the dispersion relation (7).

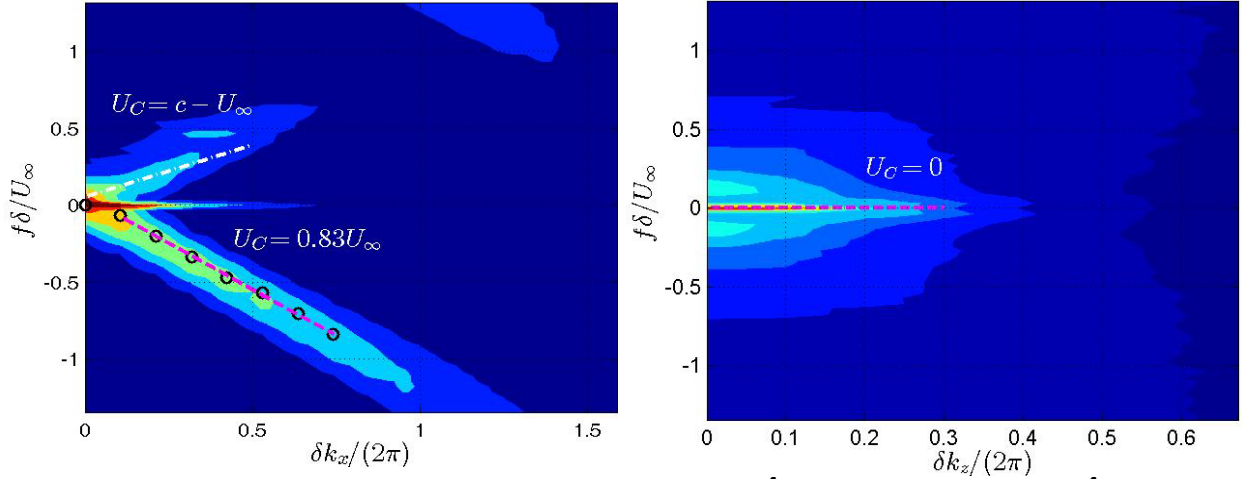


**Figure 9.** Wavefront wavenumber-frequency spectra,  $\hat{W}_{\text{NORM}}(f, k_x)$  (left) and  $\hat{W}_{\text{NORM}}(f, k_z)$  (right).  $M = 0.6$ ,  $Ap/\delta \approx 4$ .

The results are shown in Figure 9. Here the wavenumber-frequency spectrum is represented as a function of the normalized frequency  $f\delta/U_\infty$  and the normalized wavenumber,  $k_x \delta/2\pi$ . The lower ‘branch’ of the dispersion curve maxima corresponds to modes moving downstream and is related to aero-optical effects of boundary layers. For the range of aero-

optically active maxima, the dispersion curve, that is the “crest” in the wavenumber-frequency wavefront spectrum, is linear, consistent with the constant-phase-slope results in Figure 7, right plot, and confirming again that the frozen flow hypothesis is valid for aero-optical structures in the boundary layer. The value of the convective speed is 0.83 of the freestream speed agrees well with the measurements of 0.82 of the freestream speed, using the Malley Probe, shown in Figure 7, right plot. A small amount of the spectral aliasing, visible in the upper right corner in Figure 9, left plot, suggests that the temporal sampling frequency, which was 50 kHz for this set of data, would be barely enough to properly resolve the wavefront-frequency spectrum.

In addition to the lower ‘branch’, two more branches can be seen in Figure 9, left plot. A horizontal,  $f = 0$ , branch corresponds to a stationary aero-optical structure. An additional upper ‘branch’ was found to correspond to modes convecting upstream in the flow and is thought to be caused by acoustic contamination propagating upstream from the fan motor into the wind tunnel test section, as it has a velocity of approximately  $-c + U_c$ . Another indication that this branch represents low-frequency acoustic effects is that it is dominant only in the low frequency end of the spectra, consistent with the low-frequency noise emitted by the motor. In contrast, the lower branch of dispersion curve maxima shows a broadband family of forward-propagating flow aero-optical structures corresponding to the turbulent boundary layer.

Dispersion curves can also be computed for the spanwise z-direction and the result is presented in Figure 9, right plot. For the boundary layer it shows the expected result that the convective speed of the aero-optical structures in the spanwise direction is zero. However, the analysis of the spanwise dispersion relation might be useful for flows for which the convective velocity does not align with the x-direction of the aperture, and this method of analysis would allow for the computation of convective velocity components in both directions as demonstrated above.

To remove the non-boundary layer induced aberrations from further analysis, a 2-D spectral filtering method was used to remove aberrations which do not convect in the direction of freestream velocity.

#### 4.1.4 Spectral Analysis of Wavefronts

Direct measurements of deflection angle for each lenslet can be acquired using the high-speed wavefront sensor at sampling frequencies of 50 kHz, and can be directly compared to measurements made with the Malley probe. To perform this comparison, a one-dimensional “slice” of wavefront data in the streamwise direction  $W(x, t)$  was taken in the spanwise-middle of the aperture and instantaneous piston and streamwise tilt were removed from these wavefronts. Then, at a fixed streamwise location, local streamwise deflection angles were calculated as a function of time, deflection angle spectra were calculated and then averaged over all streamwise locations.

A comparison between these two different methods of computing deflection angle spectra is shown in Figure 10, left, where deflection angle spectra from 2-D wavefront data for two different apertures,  $Ap/\delta = 3.54$  and  $2.21$  are presented, along with the Malley probe spectrum. The sharp peaks at  $St_\delta = 4$  and around  $St_\delta = 10$  in the Malley probe spectrum are electronic-noise-related. Both methods give the same location and the amplitude for the maxima in the deflection angle spectra, observed at  $St_\delta \approx 1$ . Although the sampling frequency for 2-D wavefronts was 50 kHz, on the high-frequency end of the spectra there is a small energy buildup due to the spectral aliasing, implying that the wavefront frequency resolution is not high enough

to resolve *all* features which are aero-optically active within the flow. The similar spectral aliasing issue was also observed in Figure 9, left plot.

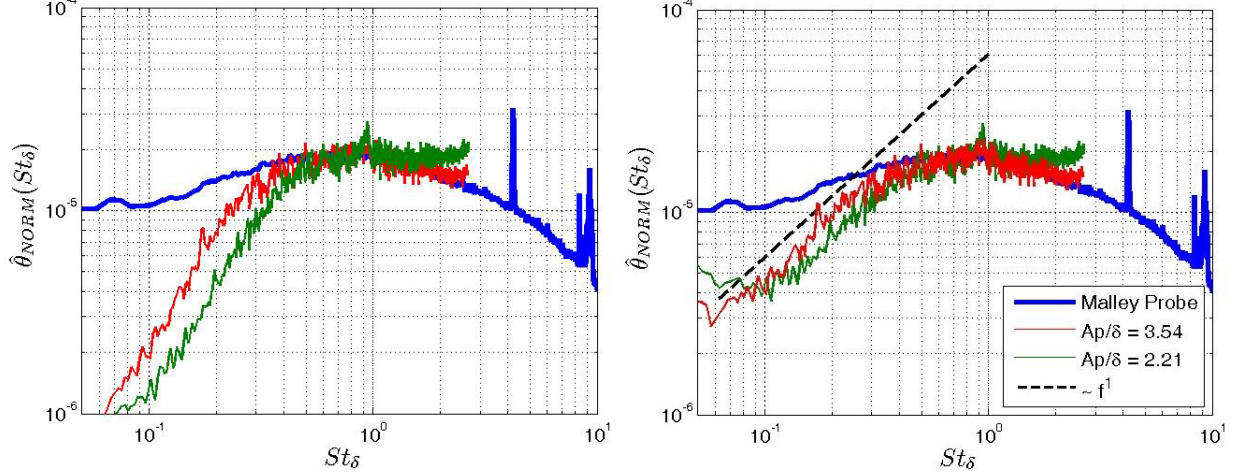


**Figure 10. Comparison between the streamwise deflection angle amplitude spectra computed from 2-D wavefront data for different apertures, original (left plot) and compensated for aperture effects (right plot) and the Malley probe deflection angle spectrum.**

Deflection angle spectra also deviate from each other at low,  $St_\delta < 0.4$ , frequencies, and this deviation appears to be a function of aperture size. To investigate the effect of aperture size on deflection angle spectra, let us recall that instantaneous global tilt was removed from each wavefront ‘slice’. Therefore, the same amount of global tilt was removed from the local deflection angle at every spatial point. The relation between the global and the local tilt was derived in [29] and it was shown that the removal of the global tilt works as a high-pass filter on the local deflection angle, with the transfer function,  $G_A(z) = [3 \sin(\pi z) - 3\pi z \cos(\pi z)] / (\pi z)^3$ , where  $z = Apf/U_C = (Ap/\delta)(U_\infty/U_C)St_\delta = 1.20(Ap/\delta)St_\delta$ . Based on this transfer function, the finite-aperture deflection angle spectra from 2-D wavefront data were corrected for aperture effects and the results are re-plotted on the right side of Figure 10. The corrected deflection angle spectra from 2-D wavefront data collapse better at the low frequency range for different aperture sizes and the low-frequency end of the amplitude spectra was found to have a slope proportional to  $f$ .

Note that the Malley probe spectrum has more energy at the low end of the spectrum, compared to the spectra from 2-D wavefront data, because it only measures the local deflection angle and inevitable contamination from mechanical vibration cannot be properly removed from the Malley probe data. On the other hand, mechanical vibrations add only a global tilt component to wavefronts and easily can be removed during data post-processing.

Streamwise spatial spectra can also be computed from wavefront data, by taking the one-dimensional wavefront ‘slices’ extracted previously,  $W(x,t)$ , computing spatial spectrum of the tilt/mean removed wavefronts at a fixed moment of time, and then averaging them over time. Since wavenumber and frequency are related via the frozen flow hypothesis by  $k_x = 2\pi f (U_c)^{-1}$ , these spectra can be converted into the frequency domain and directly compared to Malley probe wavefront spectrum, Equation (4).

Normalized 2-D wavefront spectra for different aperture sizes are plotted in Figure 11, along with the normalized spectrum using the Malley probe data. For each aperture, the corresponding spectrum agrees well with the Malley-probe spectrum, with small deviations at

the low- and the high-end of the wavefront spectrum. The deviation at the low-end of the spectrum is related to the already-discussed aperture effect [33]. The deviation at the high-end of the spectrum is due to averaging effect over finite-size lenslet aperture, also resulting in underestimating the spectra at high frequencies. In the range between  $St_\delta \approx 1$  to 10, the slope of all spectra is approximately  $\hat{W}(f) \sim f^{-5/3}$ , which is observed in other turbulent flows [34]. Deviation from this slope on the high-Strouhal number end of the spectra is the result of finite beam effects for both the Malley probe beams and wavefront lenslet diameters.

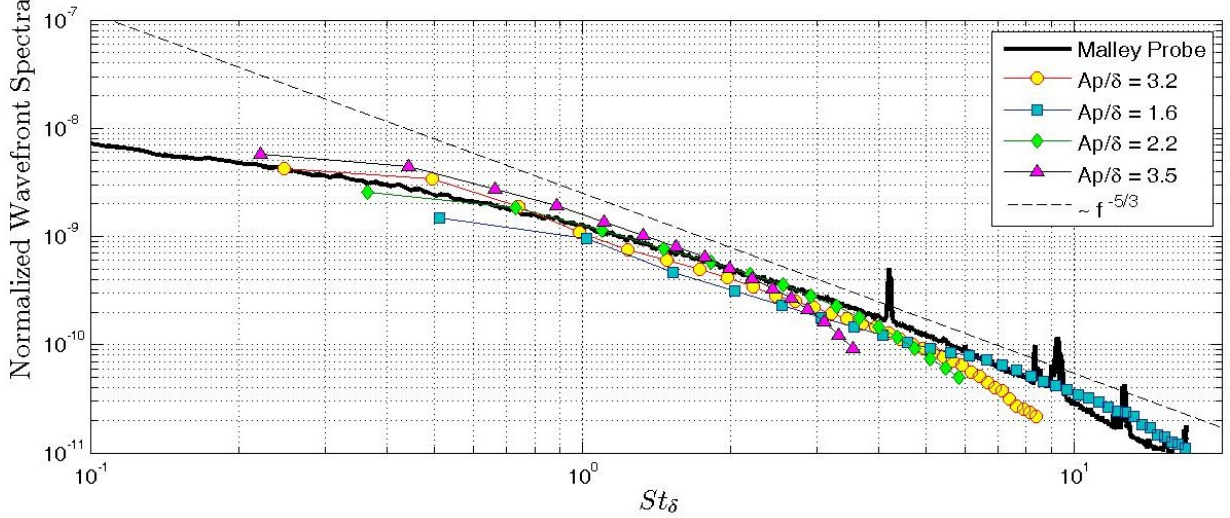


**Figure 11. Streamwise wavefront amplitude spectra scaled and plotted with Malley probe amplitude spectra using the frozen flow assumption.**

The “-5/3”-slope in the high-frequency end of the wavefront amplitude spectra for turbulent flows is a consequence of the dominance of Kolmogorov-type turbulence at small scales. Tatarski [3] showed that if the optical distortions are due to pressure or temperature fluctuations, which are proportional to a square of the velocity fluctuations,  $u'^2$ , the spectral density for *two-dimensional* wavefronts is  $\Phi(k) \sim k^{-13/3}$  for large wavenumbers. From the relation between the two-dimensional,  $\Phi(k)$ , and one-dimensional spectral densities,  $\Phi(k)d\bar{k} \sim \Phi(k)kdk \equiv |\hat{W}(k)|^2 dk$ , it follows that the *one-dimensional amplitude wavefront spectrum* should behave as  $|\hat{W}(k)| \sim (\Phi(k)k)^{1/2} \sim (k^{-13/3}k)^{1/2} = k^{-5/3}$  for large wavenumbers, or, recalling the frozen field assumption, as  $|\hat{W}(k)| \sim f^{-5/3}$  for high frequencies.

## 4.2 Models of Optical Distortions.

### 4.2.1 Aero-Optical Model for Subsonic Boundary Layer with Non-Adiabatic Wall

From the linking equation (1) it follows that if the density fluctuations and their correlation lengths across the boundary layer are known, the optical distortions can be calculated. From the ideal gas law,  $p = \rho RT$ , the density fluctuations are related to the pressure and the temperature fluctuations. As the pressure fluctuations in boundary layers were shown to be several times smaller than the temperature fluctuations [18,35,36], they can be neglected and the

temperature fluctuations can be estimated using the Strong Reynolds Analogy (SRA) [18,35,36], which presumes that  $p'$  is negligible,

$$\frac{T'}{T} = -(\gamma - 1)M^2 \frac{u'}{U},$$

where  $T$  is the static temperature,  $\gamma$  is the specific heat ratio, and  $u, U$  is the local streamwise velocity component; primes indicate fluctuating quantities and the overbar indicates mean quantities. The SRA has been empirically verified for Mach numbers up to three [36]. However, the SRA neglects fluctuations in the total temperature in a boundary layer. For turbulent boundary layers without heat transfer at the wall, this assumption does not introduce significant error [18,35,36]. But for non-adiabatic wall conditions, experimental and computational studies on have shown that fluctuations in the total temperature can be as large as 60% of the fluctuating static temperature, thus the fluctuating total temperature cannot be ignored [37,38]. Walz and van Driest proposed a form of the enthalpy equation such that  $\tilde{h} = h(\tilde{u})$ , where fluctuations in the total temperature are not ignored [35]. Carrying out the analysis similar to [35], the following relationships for mean and fluctuating static temperature are found,

$$\frac{\tilde{T}}{T_\infty} = \frac{\tilde{T}_w}{T_\infty} + \frac{\tilde{T}_{aw} - \tilde{T}_w}{T_\infty} \left( \frac{\tilde{u}}{U_\infty} \right) - r \frac{(\gamma - 1)}{2} M_\infty^2 \left( \frac{\tilde{u}}{U_\infty} \right)^2, \quad (8a)$$

$$\frac{T''}{T_\infty} = -\frac{\tilde{T}_{aw} - \tilde{T}_w}{T_\infty} \left( \frac{u''}{U_\infty} \right) - r \frac{\tilde{u}u''}{c_p}, \quad (8b)$$

where  $\tilde{T}$ ,  $\tilde{T}_\infty$ ,  $\tilde{T}_w$ , and  $\tilde{T}_{aw}$  are the Favre-averaged static, freestream, wall, and adiabatic or recovery temperatures, respectively,  $r$  is the recovery factor,  $c_p$  is the constant pressure specific heat,  $\tilde{u}$  is the Favre-averaged mean velocity, and  $u''$  is the Favre-averaged fluctuating velocity. Equation (8a) is known as the modified Crocco relation or the Walz equation. The recovery

factor is defined as  $r = \frac{\tilde{T}_{aw} - \tilde{T}_\infty}{\tilde{T}_{0_\infty} - \tilde{T}_\infty}$ . The difference between Reynolds and Favre-averaging has

been shown to be less than 1.5% for Mach numbers less than 3, thus they can be interchanged for this subsonic and low supersonic analysis [35]. Letting  $\Delta T = T_w - T_{aw}$ , and replacing fluctuating values with root-mean-square values, the following expression for  $T_{\text{rms}}$  can be found,

$$\left( \frac{T_{\text{rms}}}{T_\infty} \right)^2 = \left( \frac{u_{\text{rms}}}{U_\infty} \right)^2 \cdot \left[ \left( \frac{\Delta T}{T_\infty} \right)^2 + 2r(\gamma - 1)M_\infty^2 \left( \frac{\Delta T}{T_\infty} \right) \frac{U}{U_\infty} + \left( r(\gamma - 1)M_\infty^2 \frac{U}{U_\infty} \right)^2 \right], \quad (9)$$

where  $U$  is the mean local streamwise velocity. Thus, for negligible pressure fluctuations, the equation of state can be used to compute the density fluctuations,

$$\frac{\rho'}{\rho_\infty} = -\frac{T'}{T_\infty} \quad \longrightarrow \quad \left( \frac{\rho_{\text{rms}}}{\rho_\infty} \right)^2 = \left( \frac{T_{\text{rms}}}{T_\infty} \right)^2. \quad (10)$$

Substituting Eq. (9) into Eq. (10) gives the following relationship for  $(\rho_{\text{rms}})^2$  in terms of the velocity profile in the wall normal direction and  $\Delta T$ ,

$$\left( \frac{\rho_{\text{rms}}}{\rho_\infty} \right)^2 = \left( \frac{u_{\text{rms}}}{U_\infty} \right)^2 \cdot \left[ \left( \frac{\Delta T}{T_\infty} \right)^2 + 2r(\gamma - 1)M_\infty^2 \left( \frac{\Delta T}{T_\infty} \right) \frac{U}{U_\infty} + \left( r(\gamma - 1)M_\infty^2 \frac{U}{U_\infty} \right)^2 \right]. \quad (11)$$

Substituting Eq. (11) into the linking equation (1) results in the following relationship,

$$\text{OPD}_{\text{rms}} = B_0 \delta^* \frac{\rho_\infty}{\rho_{SL}} \left[ B_1 M^4 + B_2 \frac{\Delta T}{T_\infty} M^2 + B_3 \left( \frac{\Delta T}{T_\infty} \right)^2 \right]^{1/2}, \quad (12)$$

where,

$$\begin{aligned} B_0 &= \sqrt{2} K_{GD} \rho_{SL} (\gamma - 1), \\ B_1 &= \int_0^\infty \left[ r^2 \left( \frac{U(y) u_{\text{rms}}(y)}{U_\infty^2} \right)^2 \frac{\Lambda_y(y)}{\delta^*} \right] d\left(\frac{y}{\delta^*}\right), \\ B_2 &= \int_0^\infty \left[ \frac{2r}{(\gamma - 1)} \frac{U(y)}{U_\infty} \left( \frac{u_{\text{rms}}(y)}{U_\infty} \right)^2 \frac{\Lambda_y(y)}{\delta^*} \right] d\left(\frac{y}{\delta^*}\right), \\ B_3 &= \int_0^\infty \left[ \left( \frac{u_{\text{rms}}(y)}{U_\infty (\gamma - 1)} \right)^2 \frac{\Lambda_y(y)}{\delta^*} \right] d\left(\frac{y}{\delta^*}\right). \end{aligned}$$

Rewritten with  $A = B_0 B_1^{1/2}$ ,  $C_1 = B_2/B_1$ , and  $C_2 = B_3/B_1$ , Eq. (12) becomes,

$$\text{OPD}_{\text{rms}} = A \delta^* \frac{\rho_\infty}{\rho_{SL}} \left[ M^4 + C_1 \frac{\Delta T}{T_\infty} M^2 + C_2 \left( \frac{\Delta T}{T_\infty} \right)^2 \right]^{1/2}. \quad (13)$$

Note that Eq. (13) reduces to the previously-proposed scaling relation for subsonic speeds,  $\text{OPD}_{\text{rms}} \sim \rho \delta M^2$  [16,17], if the difference between the wall temperature and adiabatic wall temperature is zero. Equation (13) can be rearranged in the following manner,

$$\text{OPD}_{\text{rms}} = A \delta^* \frac{\rho_\infty}{\rho_{SL}} \left( M^2 + D_1 \frac{\Delta T}{T_\infty} \right) \left[ 1 + \frac{D_2}{2} \left( \frac{\Delta T/T_\infty}{M^2 + D_1 \Delta T/T_\infty} \right)^2 + H. O. T. \right], \quad (14)$$

where  $D_1 = C_1/2$  and  $D_2 = C_2 - (C_1/2)^2$ . Table 2 lists the calculated values of the five coefficients at two Mach numbers using experimentally-measured velocity profiles [26] and correlation length from [12], presented in Figure 17.

**TABLE 2: THEORETICALLY-PREDICTED  $\text{OPD}_{\text{RMS}}$  TEMPERATURE DIFFERENCE SCALING COEFFICIENTS FOR THE LOW SPEED AND TRANSONIC WIND TUNNEL FACILITIES, EQUATIONS (13) AND (14).**

	M0.12	M0.5
$A$	$1.45 \times 10^{-5}$	$1.89 \times 10^{-5}$
$C_1$	6.59	6.38
$C_2$	10.99	10.28
$D_1$	3.29	3.19
$D_2$	0.15	0.1

As the last term,  $D_2$ , in the square brackets of Eq. (14) is much less than 1, then, for positive temperature differences,

$$OPD_{rms} = A \delta^* \frac{\rho_\infty}{\rho_{SL}} \left( M^2 + D_1 \frac{\Delta T}{T_\infty} \right), \quad (15)$$

Using optical measurements from the heated/cooled wall experiments, described in Section 3.1, all these constants can be calculated. From (2), it follows that

$$\hat{\theta}(f) \sim U_\infty OPD_{rms} \quad (16)$$

Assuming that the heated and unheated boundary layers are independent, and using (16), the deflection angle spectrum for a single boundary layer can be extracted from double boundary layer spectra as,

$$\hat{\theta}(f)_{SBL, heated} = \sqrt{\left( \hat{\theta}(f)_{DBL, heated} \right)^2 - \frac{1}{2} \left( \hat{\theta}(f)_{DBL, unheated} \right)^2}.$$

Finally, using Eq. (16) and the  $OPD_{rms}$  scaling derived in Eq. (15), the deflection angle spectrum can be expressed as,

$$\hat{\theta}(f) = \frac{\delta^*}{U_\infty} \frac{\rho_\infty}{\rho_{SL}} \left( M^2 + D_1 \frac{\Delta T}{T_\infty} \right) \cdot \hat{\theta}_{norm}(St), \quad (17)$$

where  $\hat{\theta}_{norm}(St)$  is the normalized deflection angle spectrum and  $St$  is the Strouhal number,  $St = f\delta^*/U_\infty$ . Thus, the amplitude of the deflection-angle spectrum depends on the Mach number and the temperature difference. To determine the value of the  $D_1$  constant in Eq. (15), the peak of the spectrum amplitude corresponding to the maximum value near  $St = 0.1$ , was investigated as a function of temperature difference. The left plot in Figure 12 shows the peak values of the spectra amplitudes,  $\hat{\theta}_p$ , for the six tested Mach numbers and various temperature differences.

Writing Eq. (17) in terms of the peak spectrum amplitude and solving for  $D_1 \Delta T / T_\infty$  gives,

$$\frac{U_\infty}{\delta^* \rho_\infty / \rho_{SL}} \left( \frac{\hat{\theta}_{p, heated} - \hat{\theta}_{p, unheated}}{\hat{\theta}_{p, norm}} \right) = D_1 \frac{\Delta T}{T_\infty}. \quad (18)$$

The normalized peak values of the spectra amplitude are plotted versus  $\Delta T / T_\infty$  in Figure 12 (right). Of interest is that the value of  $D_1$  increases with Mach number below 0.3. The values of  $D_1$  are plotted versus the Reynolds number based on momentum thickness,  $Re_\theta$ , in Figure 13. It can be seen that the value of  $D_1$  increases until approximately a  $Re_\theta$  of 20,000; for larger  $Re_\theta$  values  $D_1$  settles on a constant value of about 2.15. The experimental values of  $D_1$  are approximately one-third less than the values shown in Table 2. Additionally, the calculated values from statistical model do not show the strong Reynolds number dependence seen in the experimental data at lower  $Re_\theta$  values. A potential source for this discrepancy could be that the same correlation length function [12] was used for both the Mach 0.12 and 0.5 cases, as changes in the correlation length function between the corresponding  $Re_\theta$  values might account for the  $Re_\theta$  dependence, and transition effects were not considered.

Shown in Figure 14, left, are the normalized spectra amplitudes at Mach 0.4 for two temperature difference extremes,  $\Delta T \sim 0$  and 19.2 K, where the temperature difference term has been neglected in the normalization (i.e.  $D_1 = 0$ ). The right plot in Figure 14 shows the normalized spectra amplitudes for the same conditions but now including the temperature difference in the normalization with  $D_1$  as found by Eq. (18) and Figure 12, right. The proposed

normalization for temperature dependence from Eq. (17) shows an excellent collapse of the experimental data. As previously discussed, the two cases show some disagreement in the slope of the roll-off at higher frequencies. However, the location of the peak spectrum value near  $St \sim 0.1$  is not affected with the change in temperature difference, and moreover the shape of the spectrum in general was not altered, but rather it was just linearly shifted vertically with  $\Delta T$ . This suggests that the effect of temperature difference, at least in the regime studied, did not significantly change the overall statistical properties of the boundary layer structures, but only amplified the fluctuating density values within the structures. Also, the spectrum was linearly amplified across a large range of  $St$  values, which suggests that the temperature difference equally affected a broad scale of structure sizes.

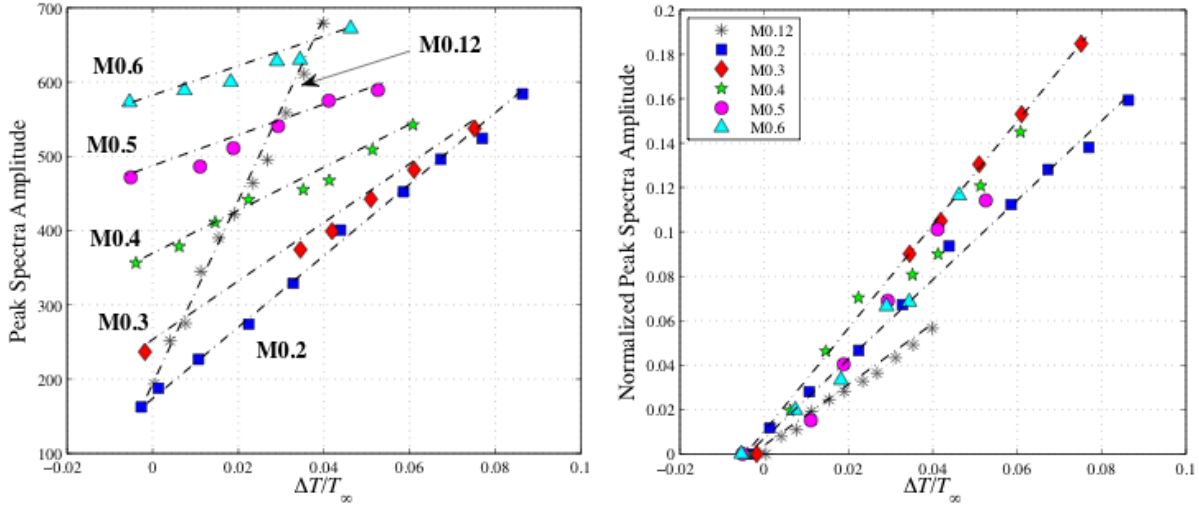


**Figure 12.** (left) Peak values from the spectra amplitude at six Mach numbers and a range of temperature differences. (right) Normalized peak values of the spectra amplitude, Eq. (18), plotted versus  $\Delta T/T_\infty$ .

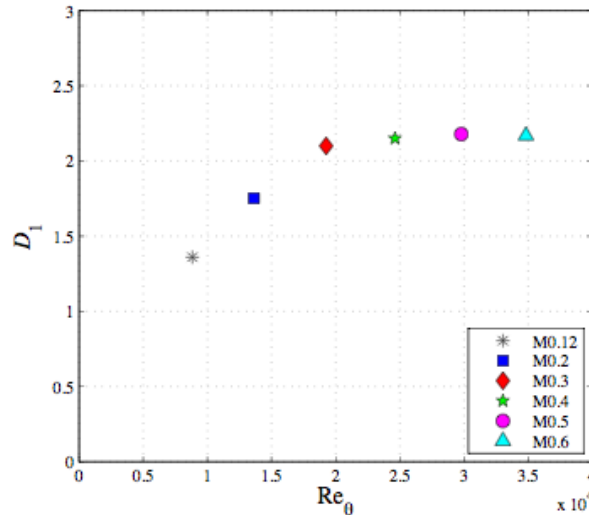


**Figure 13.**  $D_1$  plotted versus Reynolds number based on momentum thickness.

To compute OPDrms for both the heated and cooled boundary layer, the deflection angle time history signal was high-pass filtered, integrated via equation (2), and apertured into 0.25 m

windows. The root mean square of the  $OPD(x)$  was ensemble-averaged over all windows to give the mean  $OPD_{rms}$  for each Mach number and temperature difference. Finally, the effect of second boundary layer over the unheated wall was removed to calculate  $OPD_{rms}$  values for the single heated boundary layer. Figure 15 shows the  $OPD_{rms}$  data for the heated wall experiments plotted versus the linear scaling relationship of equation (15). It is evident from this figure that the linear scaling relationship successfully collapses the  $OPD_{rms}$  values over a wide range of Mach numbers and positive temperature differences. The data also shows that the scaling relationship is facility independent because the data taken in the low speed tunnel ( $M = 0.12$ ) and in the transonic tunnel ( $M = 0.2, 0.3, 0.4, 0.5,$  and  $0.6$ ) scale with the same factors. The slope of the  $OPD_{rms}$  data was found to be  $A = 1.7 \times 10^{-5}$ , which is consistent with the previously reported values for adiabatic boundary layers [17]. Further, it is apparent from these results that a positive mismatch between the wall temperature and the adiabatic wall temperature can greatly affect the  $OPD_{rms}$  value that an optical system would experience. Thus, the effect of positive temperature difference cannot be ignored in optical measurements of the turbulent boundary layer.

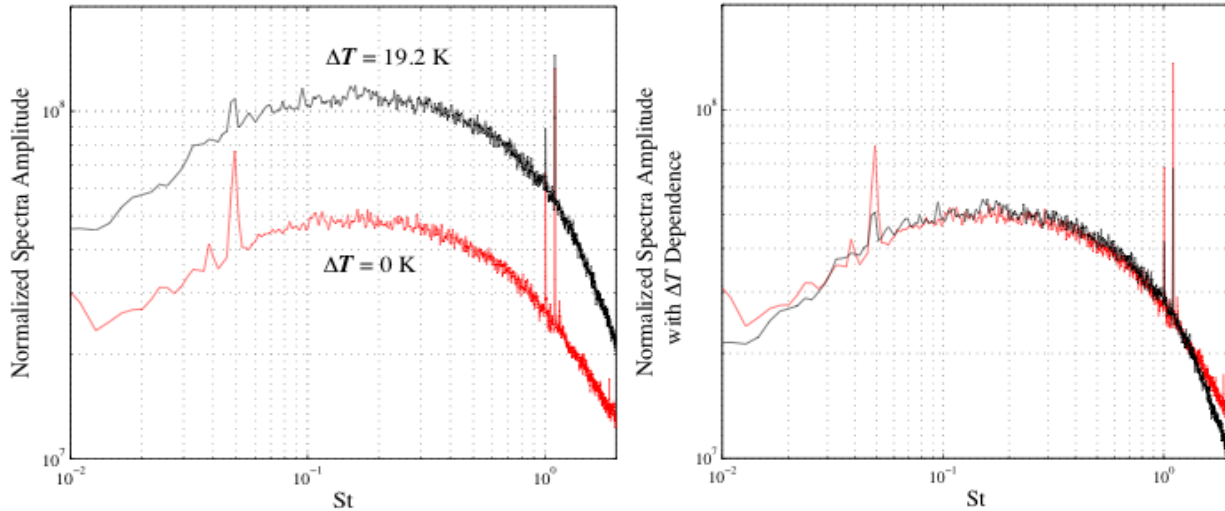


**Figure 14. (left) Normalized spectra amplitude, Eq. (17), neglecting the temperature dependence (i.e.  $D_1 = 0$ ), for the Mach 0.4 turbulent boundary layer at two  $\Delta T$  extremes, 0 and 19.2 K. (right) Normalized spectra amplitude with temperature dependence included at the same conditions.**

For negative temperature differences, the second term in (14) cannot be ignored, so the full scaling relationship (13) should be used instead. The  $OPD_{rms}$  data are plotted versus the full scaling relationship in Figure 16, left plot. The values of the  $C_1$  coefficients were found using the  $D_1$  constants from the peak spectra analysis ( $C_1 = 2 D_1$ ). The  $C_2$  coefficients were evaluated from a linear interpolation of the calculated values at  $M = 0.12$  and  $0.5$  presented in Table 2. As with the linear scaling relationship (15), the full  $OPD_{rms}$  scaling successfully captures the general trends of the experimental data. The coefficient  $A$  was found to be  $1.6 \times 10^{-5}$ , again consistent with the earlier results [17].

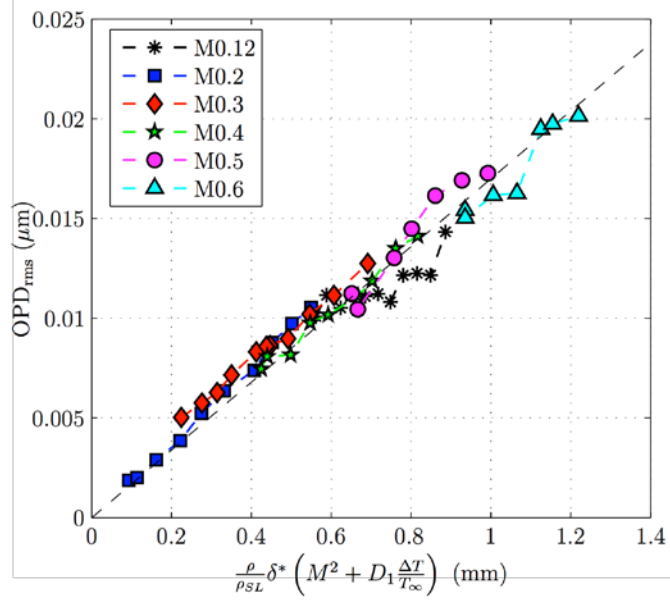


**Figure 15.**  $OPD_{rms}$  versus the scaling relationship given by Eq. (15) and the  $D_1$  constants found by the spectra analysis for five Mach numbers and several positive temperature differences. The constant of proportionality,  $A$ , was found to be  $1.7 \times 10^{-5}$ .

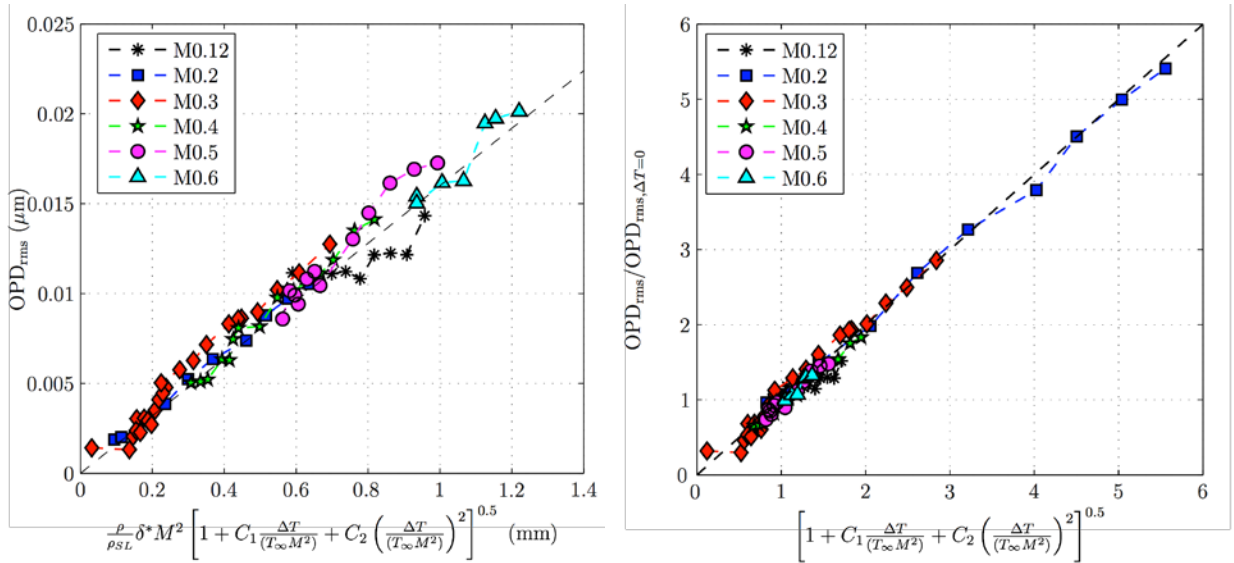


**Figure 16: Left:**  $OPD_{rms}$  versus the full scaling relationship given by equation (13). **Right:**  $OPD_{rms}$  normalized by the  $OPD_{rms}$  value with  $\Delta T = 0$  plotted versus equation (19) for all tested Mach numbers and temperature differences.

One final insight can be found by normalizing the full  $OPD_{rms}$  scaling relationship by the  $OPD_{rms}$  value at  $\Delta T = 0$ . Factoring out  $M^2$  from the right hand side of the full  $OPD_{rms}$  scaling equation and recalling that  $OPD_{rms}^{\Delta T=0} = A \frac{\rho_{\infty}}{\rho_{SL}} \delta^* M^2$ , gives the normalized  $OPD_{rms}$  expression,

$$\frac{\text{OPD}_{\text{rms}}}{\text{OPD}_{\text{rms}}^{\Delta T=0}} = \left[ 1 + C_1 \frac{\Delta T}{(T_\infty M^2)} + C_2 \left( \frac{\Delta T}{(T_\infty M^2)} \right)^2 \right]^{\frac{1}{2}} \quad (19)$$

From here it follows that negative temperature differences  $\Delta T/T_\infty = -\frac{1}{2}(C_1/C_2)M^2$  would result in the minimum optical aberrations. Figure 16, right plot, shows the normalized  $\text{OPD}_{\text{rms}}$  versus equation (19) for the six tested Mach numbers and all temperature differences. The strong effect of the difference between the wall and adiabatic wall temperature is apparent in this normalized  $\text{OPD}_{\text{rms}}$  figure. For instance, at  $M = 0.2$ , with the heated wall  $28^\circ\text{C}$  above the adiabatic wall temperature, the optical aberrations were increased by a factor of 5.5 times; at  $M = 0.3$ , with a temperature difference of  $21^\circ\text{C}$ , the optical aberrations were increased by three times. The opposite trend was seen for negative temperature differences. With a difference of  $-12^\circ\text{C}$  at  $M = 0.3$ , the optical aberrations in the turbulent boundary layer were decreased by nearly 80%. This is a dramatic decrease in the magnitude of optical aberrations and it provides a promising passive way to significantly reduce aero-optical distortions caused by turbulent boundary layers.

The only other model for including temperature effects in aero-optical boundary-layer distortions is the model proposed by Wyckham and Smits [18],

$$\text{OPD}_{\text{rms}} = C_w K_{GD} \rho_\infty \delta M_\infty^2 \sqrt{C_f} r_2^{-3/2}, \quad (20)$$

where  $r_2 = 1 + \frac{\gamma-1}{2} M_\infty^2 [1 - r(U_c/U_\infty)^2]$  for adiabatic walls, or  $r_2 = 0.5(T_w/T_\infty + 1)$  for heated or cooled walls, where  $r$  is the recovery factor. Experimentally,  $C_w$  was found to be between 0.7 and 1.0 for a range of Mach numbers between 0.8 and 7.8. From their model it follows that optical aberrations are inversely related to the wall temperature; their model predicts that the value of  $\text{OPD}_{\text{rms}}$  will *decrease* as the wall temperature is *increased*. Clearly, the experimental data presented in this section pointedly contradicts this result. Close inspection shows that Wyckham-Smith model is based upon the SRA, not the ‘‘extended’’ SRA, and assumes that total enthalpy is constant throughout the boundary layer, and therefore does not allow the total temperature to vary.

#### 4.2.2 Model for Aero-Optical Distortions for Compressible Boundary Layers

While the model Eq. (13) correctly predicts aero-optical aberrations of the subsonic boundary layer with heated and cooled walls, it does not take into account spatial changes of the *mean* density and temperature profiles across the boundary layer and, as it will be shown later in this section, over-predicts the level of aero-optical distortions for a supersonic boundary layer. Let us re-visit the model derivation in order to improve its predictions for a large range of Mach numbers. For simplicity, we will derive the modified model for adiabatic walls only.

The equation of state  $P = \rho RT$  can be re-written as,

$$\frac{\rho_{\text{rms}}(y)}{\rho(y)} = -\frac{T_{\text{rms}}(y)}{T(y)}, \rightarrow \rho_{\text{rms}}(y) = -T_{\text{rms}}(y) \frac{\rho_\infty}{T_\infty} \frac{\rho(y)/\rho_\infty}{T(y)/T_\infty} = -T_{\text{rms}}(y) \frac{\rho_\infty}{T_\infty} \frac{1}{(T(y)/T_\infty)^2} \quad (21)$$

Using the Morkovin scaling for compressible boundary layer [19],  $\sqrt{\frac{\rho(y)}{\rho_w} \frac{u_{\text{rms}}(y)}{u_\tau}} = g(y/\delta)$ ,

where  $u_\tau$  is the skin friction velocity and  $\rho_w$  is the density near the wall, assuming the self-similarity of the mean velocity profile,  $U(y)/U_\infty = f(y/\delta)$  and substituting both

approximations into (21), we get the following expression for density fluctuations across the boundary layer,

$$\rho_{rms}(y) = \rho_\infty \frac{rU_\infty f(y/\delta)u_\tau \sqrt{\rho_w / \rho(y)}g(y/\delta)}{c_p T_\infty (T(y)/T_\infty)^2} = \rho_\infty \frac{(\gamma-1)rU_\infty f(y/\delta)U_\infty \sqrt{C_f/2} \sqrt{T(y)/T_0} g(y/\delta)}{a_\infty^2 (T(y)/T_\infty)^2} = \quad (22)$$

$$\rho_\infty \frac{(\gamma-1)rM_\infty^2 \sqrt{C_f/2} f(y/\delta) \sqrt{T(y)/T_0} g(y/\delta)}{(T(y)/T_\infty)^2} = \rho_\infty \frac{(\gamma-1)rM_\infty^2 \sqrt{C_f/2} \sqrt{T_\infty/T_0} f(y/\delta) g(y/\delta)}{(T(y)/T_\infty)^{3/2}}$$

Using the adiabatic relation between the static temperature and the velocity, equation (22) can be finally written as,

$$\rho_{rms}(y) = \rho_\infty (\gamma-1)rM_\infty^2 \sqrt{C_f/2} \left(1 + \frac{(\gamma-1)}{2} M_\infty^2\right)^{=1/2} \frac{f(y/\delta)g(y/\delta)}{\left(1 + \frac{(\gamma-1)}{2} M_\infty^2 [1 - f^2(y/\delta)]\right)^{3/2}}$$

To estimate the level of optical distortions by boundary layers, the estimated density fluctuations are substituted into the linking equation (1) to get the following equation for  $OPD_{rms}$ ,

$$OPD_{rms} = \sqrt{2}K_{GD}\rho_\infty\delta(\gamma-1)rM_\infty^2\sqrt{C_f/2}\left(1 + \frac{(\gamma-1)}{2}M_\infty^2\right)^{=1/2} \times$$

$$\left(\int_0^\infty \left[\frac{f(y/\delta)g(y/\delta)}{\left(1 + \frac{(\gamma-1)}{2}M_\infty^2[1 - f^2(y/\delta)]\right)^{3/2}}\right]^2 \frac{\Lambda_y(y/\delta)d(y/\delta)}{\delta}\right)^{1/2}, \text{ or} \quad (23)$$

$$OPD_{rms} = C(0)K_{GD}\rho_\infty M_\infty^2 \delta \sqrt{C_f} \frac{C(M_\infty)}{C(0)} = BK_{GD}\rho_\infty \delta \sqrt{C_f} F_1(M_\infty)$$

where

$$C(M_\infty) = (\gamma-1)r \left(1 + \frac{(\gamma-1)}{2} M_\infty^2\right)^{=1/2} \left(\int_0^\infty \left[\frac{f(y/\delta)g(y/\delta)}{\left(1 + \frac{(\gamma-1)}{2} M_\infty^2 [1 - f^2(y/\delta)]\right)^{3/2}}\right]^2 \frac{\Lambda_y(y/\delta)d(y/\delta)}{\delta}\right)^{1/2}, \quad (24)$$

$B = C(0)$ ,  $F_1(M_\infty) = M_\infty^2 C(M_\infty) / C(0)$  and  $\Lambda_y(y/\delta)$  is a wall-normal density correlations length; two different correlation lengths were used to estimate  $OPD_{rms}$ ,  $\Lambda_y^{(1)}(y/\delta)$  is provided by Gilbert [12] and  $\Lambda_y^{(2)}(y/\delta)$  is measured by Rose and Johnson [39].

Note, that both the model (23) and the Wyckham-Smith model (20) have the same functional form,  $OPD_{rms} \sim K_{GD}\rho_\infty\delta\sqrt{C_f}$ , but a different Mach-number-dependent function,

$F_1(M_\infty)$  for the modified model Eq. (23) and  $F_2(M_\infty) = M_\infty^2 \left(1 + \frac{\gamma-1}{2} M_\infty^2 [1 - r(U_c/U_\infty)^2]\right)^{-3/2}$  for the model Eq. (20). To calculate  $F_1(M_\infty)$  from (24), experimentally-measured velocity profiles for a  $M = 0.5$  boundary layer were used; Figure 17 shows the wall-normal variation of  $f(y/\delta)$ ,  $g(y/\delta)$ ,  $\Lambda_y^{(1)}(y/\delta)$  and  $\Lambda_y^{(2)}(y/\delta)$ .

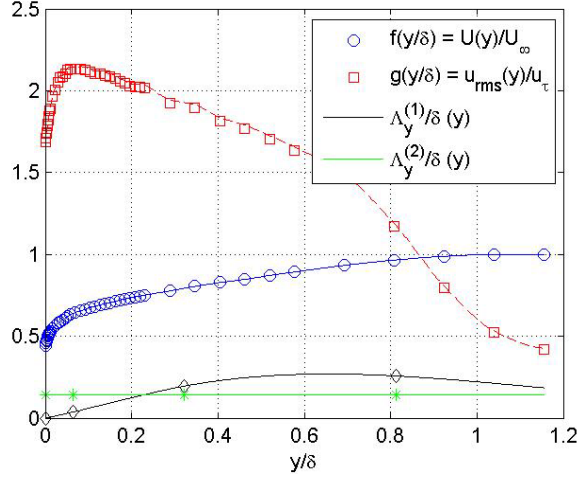


**Figure 17. Normalized mean and fluctuation velocity profiles and the two tested density correlation functions (from [12] and [39]).**

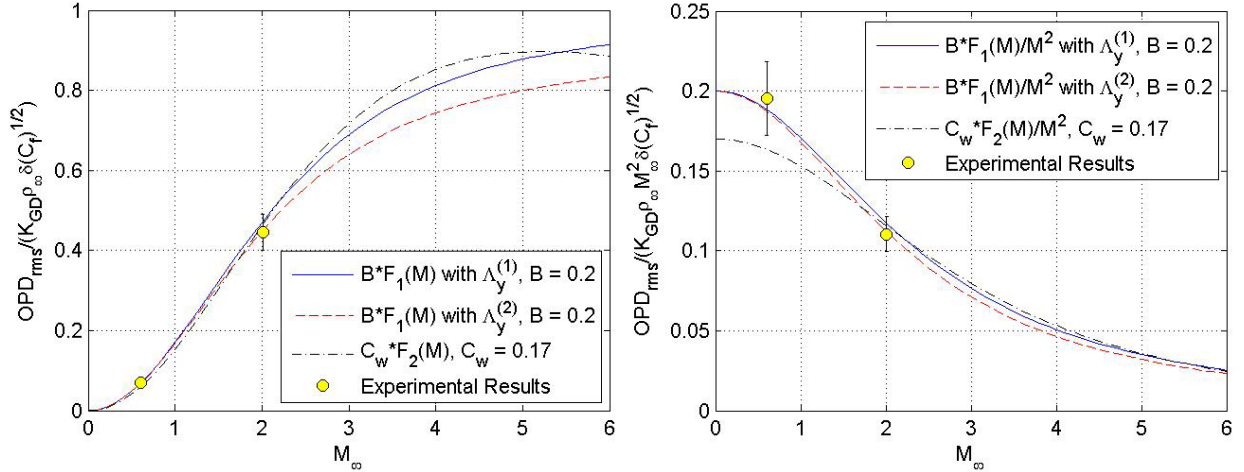


**Figure 18. Comparison between theoretical predictions, Eqs. (ED4a,b) and (23) and experimental data:  $OPD_{rms} / (K_{KD} \rho_{\infty} \delta(C_f)^{1/2})$  (left) and  $OPD_{rms} / (K_{KD} \rho_{\infty} M_{\infty}^2 \delta(C_f)^{1/2})$  (right) as a function of Mach number.**

To compare predictions from both models over the range of Mach numbers, constants  $B$  and  $C_w$  were adjusted to best match the experimental data for  $M = 0.6$  and  $2.0$  boundary layers;  $B \cdot F_1(M_{\infty})$ , with  $B = 0.20$  for two different correlation length functions,  $\Lambda_y^{(1)}(y/\delta)$  and  $\Lambda_y^{(2)}(y/\delta)$ , and  $C_w \cdot F_2(M_{\infty})$ , with  $C_w = 0.17$ , are plotted in Figure 18, along with properly scaled experimental data. The model Eq. (23) shows some dependence on the chosen correlation length function, as  $B \cdot F_1(M_{\infty})$  with  $\Lambda_y^{(1)}(y/\delta)$  is consistently above  $B \cdot F_1(M_{\infty})$  with  $\Lambda_y^{(2)}(y/\delta)$ , as the density correlation lengths  $\Lambda_y^{(2)}(y/\delta)$  are smaller than  $\Lambda_y^{(1)}(y/\delta)$ ; note that this difference can be somewhat minimized by adjusting the constant  $B$  for each function. Both models (23) and (20) agree fairly well over a range of supersonic Mach numbers between 1 and 6; however, the model (20) under-predicts the level of optical aberration for the subsonic boundary layer by 10-15% for subsonic Mach numbers from 0 to 1. Numerical integration of Eq.

(24) gives the value of  $B_{theory} = 0.22$  using  $\Lambda_y^{(1)}(y/\delta)$ , and the value of  $B_{theory} = 0.19$  using  $\Lambda_y^{(2)}(y/\delta)$ ; these values are close to the experimental value of  $B = 0.20$ .

The good agreement between the experimentally-measured and theoretically-predicted values of B-constants verified the use of the linking equation and underlying assumption that the pressure fluctuations inside the boundary layer do not significantly affect time-averaged aero-optical distortions and the adiabatic cooling-heating is the main mechanism for aero-optical aberrations.

As a final remark, since the optical aberrations are related to density fluctuations, the optical-structure convective speed can be estimated by using a weighted-integral, with  $\rho_{rms}(y)$  as a weighting function,

$$U_c = \int_0^{\infty} \rho_{rms}(y)U(y)dy / \int_0^{\infty} \rho_{rms}(y)dy .$$

Calculations of the convective speed as a function of the freestream Mach number are presented in Figure 19; also in the same Figure, experimentally-measured convective speeds for  $M = 0.6$  and  $M = 2.0$  boundary layers are presented for comparison. While the modified model slightly over-predicts the absolute value of the convective speed, it does correctly predict the experimentally-observed increase of the convective speed with the Mach number.

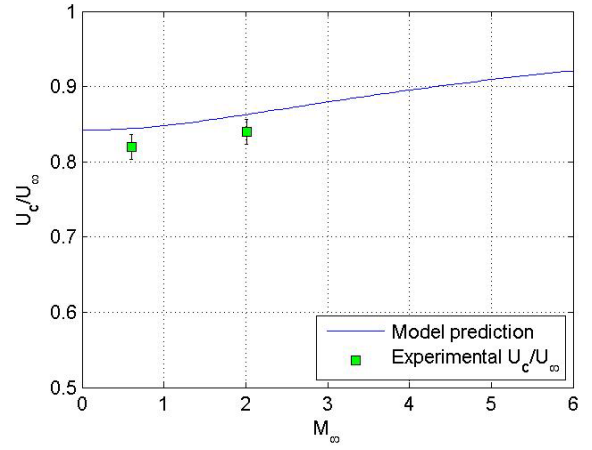


**Figure 19. Model-calculated optical-structure convective speeds and experimental results.**

### 4.3 Finite Aperture Affects

As shown in Section 3.5, for very large apertures  $Ap \gg 10\delta$ , BL streamwise growth cannot be ignored and, for an infinitely-large aperture, aero-optical aberrations caused by boundary layers will be infinite. However, for most practical applications, aperture sizes are on the order of several boundary-layer thicknesses and, in this case, the boundary-layer can be assumed to be homogeneous in the streamwise direction and the frozen-field assumption can be used to trade the streamwise coordinate,  $x$ , and time,  $t$ ,  $x = -U_C t$ .

In Section 4.1.1 it was shown that knowing the local deflection-angle temporal spectrum, we can compute  $OPD_{rms}$  for any aperture, less than  $10 \delta$ 's, using Eq. (5). Experimentally-obtained deflection-angle spectrum, see Figure 10, was approximated using an empirical fit,

$$\hat{\theta}^{fit}(St_\delta) = \hat{\theta}_{peak} \frac{(St_\delta)^m}{1 + (St_\delta / St_{peak})^{\frac{2}{3}+m}} \quad (25)$$

where  $\hat{\theta}_{peak}$  is the peak amplitude,  $St_{peak} \approx 1$  is the peak location of the curve fit in Strouhal number space, and  $m$  is a real number which characterizes the behavior of the low-frequency end of the 1-D spectra,  $\hat{\theta}(St_\delta) \sim (St_\delta)^m$ . Based on finite-aperture-corrected spatially- and temporally-resolved wavefront measurement shown in Figure 20, the value of  $m$  it has been estimated from the low-frequency wavefront measurements to be  $m = 1.1$ .

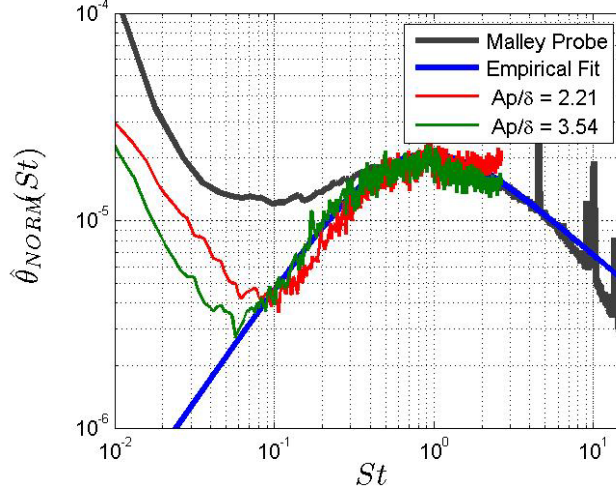


**Figure 20: Finite aperture corrected deflection angle spectra compared with the empirical fit (25).**

As seen in Figure 20, the empirical fit does a good job of modeling the measured deflection-angle spectrum in the area of the peak location, as well as in the finite-aperture-corrected low-frequency end of the spectra, except the very low frequencies  $St_\delta < 0.1$ . This very low end would affect wavefront statistics only for apertures larger than  $10 \delta$ s, where the presented spectra-based analysis would fail anyway due to streamwise evolution effects discussed in Section 3.5.

Using the empirical fit, Eq. (25) and substituting it into Eq. (5), the aperture effects on  $OPD_{rms}$  can be computed for a range of different apertures. Results are presented in Figure 21, along with experimental 2-D wavefront results, and show very good agreement. The level of aero-optical distortions is a monotonic function of  $Ap/\delta$  and varies significantly for  $Ap/\delta < 7$ . For larger apertures, the normalized  $OPD_{rms}$  approaches the value of 0.18, which is consistent with the previous measurements and theoretical predictions at this range of subsonic speeds, see Figure 18. This agreement validates the frozen field assumption used to analyze the Malley probe data for boundary layers.

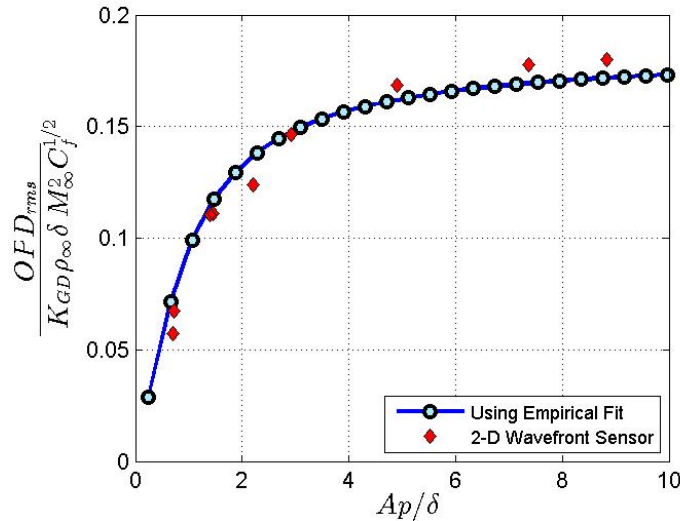


**Figure 21: Comparison of predicted and measured  $OPD_{rms}$  for different aperture sizes.**

Note that for very large apertures one needs to account for the boundary layer growth over the aperture, and therefore technically the levels of aero-optical distortions become infinite for infinite apertures. However, in practice aperture sizes are typically small to satisfy the streamwise homogeneous assumption discussed in Section 3.5.

#### 4.4 Optical Correlation Results

Streamwise and spanwise wavefront correlation data can be obtained from the 2-D wavefront data by computing autocorrelation maps for a large number of instantaneous wavefront realizations, and then averaging these instantaneous autocorrelation maps to calculate normalized time-averaged autocorrelation functions,  $\rho(\Delta x, \Delta z) = R(\Delta x, \Delta z) / R(\Delta x=0, \Delta z=0)$  for a number of different aperture values. Examples of these data for two different aperture sizes are presented in Figure 22. Aperture effects primarily effect the streamwise correlation. Below we will discuss the streamwise and the spanwise correlation functions separately.

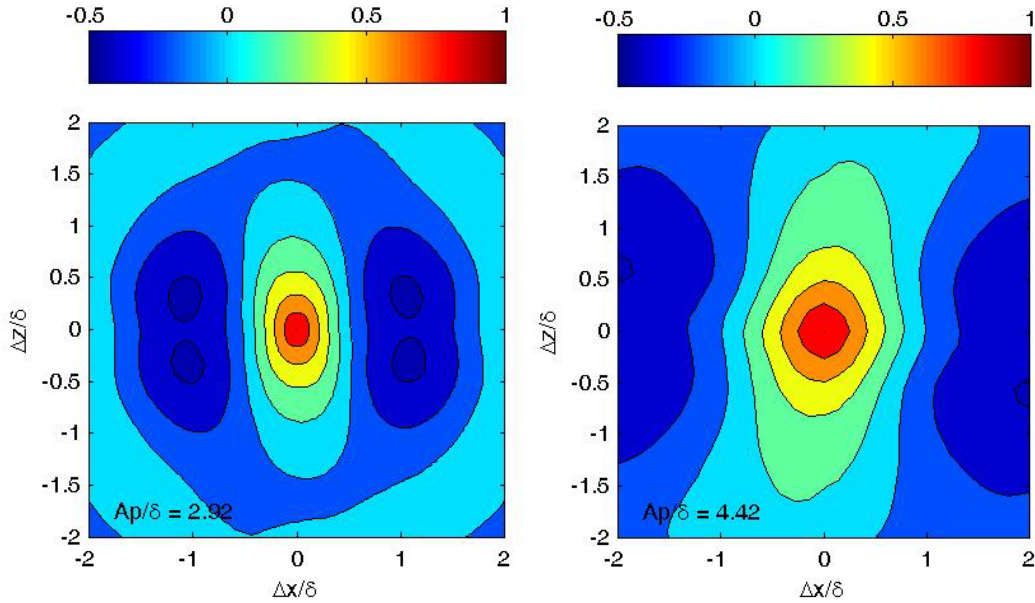


**Figure 22: Time-averaged auto correlation maps for 2-D wavefront measurements for different aperture sizes,  $Ap/\delta = 2.92$  (left) and  $Ap/\delta = 4.42$  (right).**

##### 4.4.1 Streamwise Correlation Length

From experimental correlation function, streamwise correlation functions  $\rho_x(\Delta x/\delta) = 0$  were computed. Also, the streamwise correlation function can be computed using the streamwise deflection angle spectra. Including aperture effects, the streamwise correlation function becomes,

$$R(\Delta x) = 2U_c \int_0^{\infty} AF(Ap, f) \frac{P_{\theta}(f)}{(2\pi f)^2} \exp(2\pi i f / U_c) df \quad (26)$$

From here, the streamwise correlation function can be computed using the empirical fit (25). The correlation functions were calculated and the results of both experimental measurements using 2-D wavefronts and correlation functions computed from the deflection-angle spectra are presented in Figure 23, left plot. The experimentally-obtained and computed correlation functions show good agreement up until approximately the first zero crossing. The reason of

discrepancy between computed and experimental results for large streamwise separations is most probably due to experimental error and, in lesser degree, the spectrum mismatch at very low end of the deflection-angle spectrum, observed in Figure 20. A comparison between streamwise correlation predictions from the present study and correlation functions obtained from CFD simulations by Wang and Wang [40] are shown in Figure 23, right plot. These data show good agreement up until approximately the first zero crossing as well.

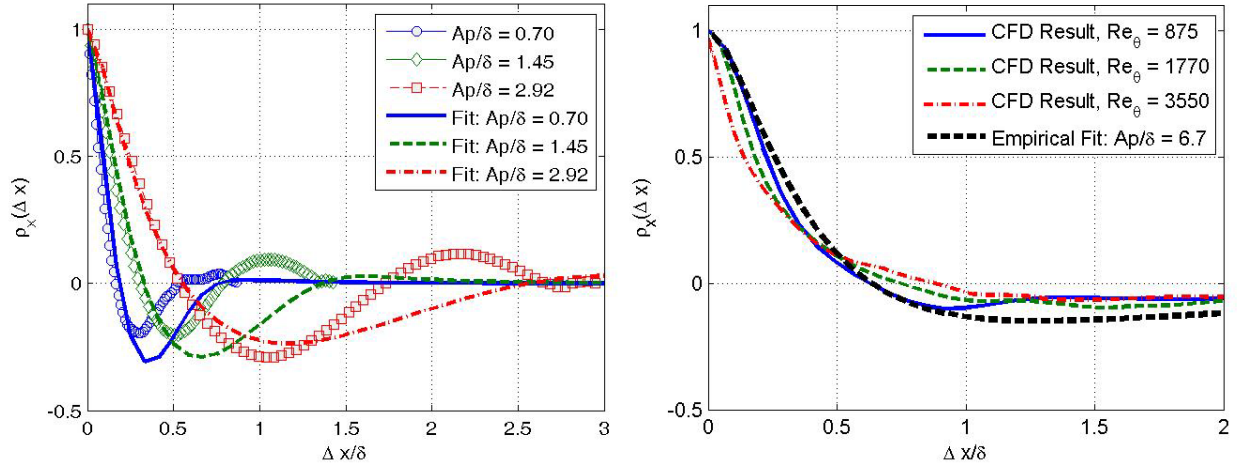


**Figure 23: Left: Streamwise wavefront correlation functions using analytical prediction (26) and experimental 2-D wavefront measurements. Right: comparison between the analytical prediction and CFD simulations [40] for  $Ap/\delta = 6.70$  (right).**

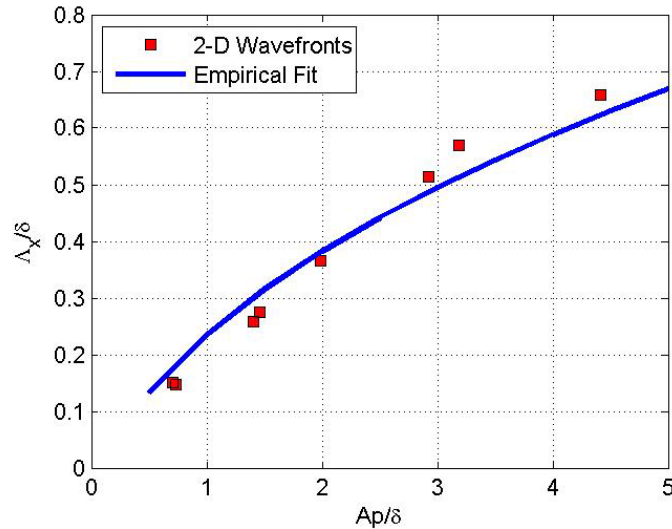


**Figure 24: Streamwise correlation length for different aperture sizes.**

A comparison of all the results shows that the finite aperture size has a significant effect on the measured correlation function for boundary layer wavefronts. The effect of finite aperture size can be further characterized by computing the integral correlation lengths for each aperture correlation function. Correlation length,  $\Lambda_x$ , was computed by the equation

$$\Lambda_x\left(\frac{Ap}{\delta}\right) = \int_0^{\xi} \rho_x\left(\frac{\Delta x}{\delta}; Ap\right) d\left(\frac{\Delta x}{\delta}\right)$$

where  $\xi$  is the first value of  $Ap/\delta$  which satisfies  $\rho_x(\xi)=0$  (i.e. the first zero-crossing point). Computed correlation lengths for both experimental and finite-aperture model predictions are presented in Figure 24. It was found that the length scale for both the experimental data and simulated correlation functions were in good agreement.

#### 4.4.2. Spanwise Correlation

Spanwise correlation functions  $\rho_z(\Delta z/\delta) = 0$  were also computed from the time-averaged correlation maps obtained from 2-D wavefront measurements, and the resulting functions are presented in Figure 25. As we might expect from the streamwise correlation function results, the spanwise correlation function appears to be strongly dependent on aperture size. Malley probe and wavefront measurements from previous aero-optical studies from [17,26] and numerically-simulated wavefronts [40] are presented along with the 2-D wavefront data. While the 2-D wavefront data and 2-D computational data presented all appear to follow similar trends with regard to spanwise aperture size, Malley probe measurements do not match the 2-D wavefront data. This difference is likely due to the fact that while the Malley probe measurements were direct measurements of spanwise correlation, they are merely detecting average wavefront slope correlation in the spanwise direction. This discrete measurement method may be failing to capture some of the more complex dynamics of the system which are better resolved with the good spatial resolution available with the 2-D wavefront sensor.

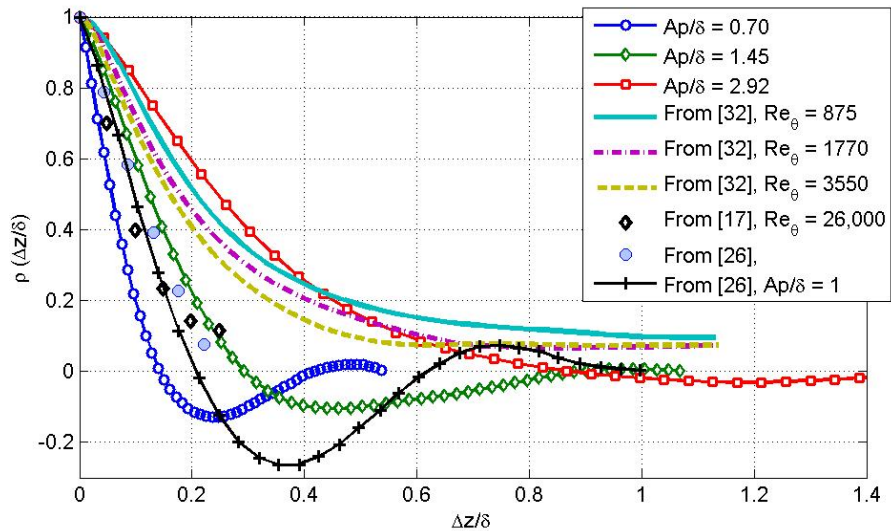


Figure 25: Spanwise correlation functions for different finite spanwise apertures  $\Lambda_z$

#### 4.5 Instantaneous Far-Field Intensity Drop-Outs.

As mentioned in the introduction, because the time-averaged Strehl ratios for beams transmitted through most attached turbulent boundary layers are usually quite high, turbulent boundary layers have always been presumed to be an aero-optic non-issue; however in [16] the issue of intermittent dropouts was raised. Additional research in recent years [17] is yielding a more complete 2-D picture of the aberrating boundary-layer structures, and while the general comments regarding time-averaged Strehl ratio remain unchanged, the warnings of possible dropout problems now seem more likely to cause a serious deterioration of transmitted laser communication signals.

If the optical wavefront has a normal distribution in space over the aperture, then the Maréchal formula [41] to calculate the *instantaneous* Strehl Ratio was shown to be exact for any  $OPD_{rms}$  [42],

$$SR(t) = \exp\left(-\left[\frac{2\pi OPD_{rms}(t)}{\lambda}\right]^2\right) \quad (27)$$

Detailed analysis of both 1-D and 2-D wavefronts over the range of aperture sizes [31] had revealed that *spatially* wavefronts have a normal distribution regardless of the aperture size. Thus, for turbulent boundary layers the instantaneous Strehl Ratio,  $SR(t)$ , is directly related to the instantaneous  $OPD_{rms}(t)$  via Eq. (27).

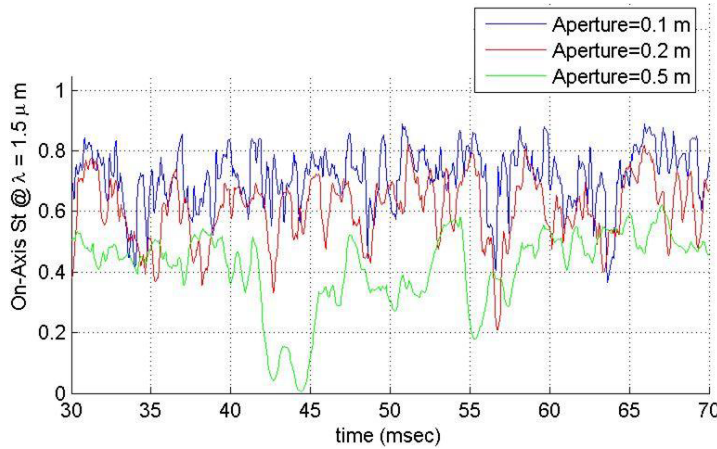


**Figure 26. Instantaneous far-field Strehl ratio vs time for laser beams propagated through boundary layers for different beam apertures of 0.1, 0.2 and 0.5 m for a  $\delta = 20$  cm thick boundary layer and a  $1.5 \mu\text{m}$  laser.**

Example of the *time-resolved* Strehl ratio as a function of time are plotted in Figure 26 for communication laser wavelength of  $1.5 \mu\text{m}$  for three aperture sizes,  $Ap = 10, 20$  and  $50$  cm; the experimentally measured OPDs were re-scaled in amplitude for boundary-layer thickness of  $\delta = 20$  cm which represent distances of approximately 12 m aft of the nose of the aircraft for  $M = 0.8$ . While the average intensity is still relatively high in all cases, it is clear that there are many dropouts, lasted few milliseconds, especially for larger apertures. From a laser-based communication point of view, these energy drop-outs might translate into a loss of several Gigabytes of data during each drop-out, inevitably slowing the communication link, since the lost chunks of data, must be constantly retransmitted. It should also be pointed out that these predictions are based on the beam being projected normal to the boundary layer; the  $OPD$  increases when the beam is projected through the boundary layer at oblique angles [26,43], thus making the intensity drop-out problem even worse. Also, it should be remembered that in all of these cases the tip/tilt was removed over the aperture which acts as a high-pass filter, as discussed in Section 4.1.2. Thus the dropouts for the smaller apertures are reduced by the tip/tilt removal until the aperture size becomes larger than the aero-optical structure size, in which case the tip/tilt removal no longer reduces the  $OPD$ .

The statistical distribution of  $OPD_{rms}(t)$  in time is more relevant than the time traces of  $OPD_{rms}(t)$ . Figure 27, left, shows a probability density function for the  $OPD_{rms}(t)$  for the aperture of  $Ap = 10\delta$  for  $M = 0.4$  and  $0.5$ . The shape of the PDF at each Mach number is well-approximated by a log-normal probability density function,

$$PDF(OPD_{rms}) = \frac{1}{OPD_{rms}s\sqrt{2\pi}} \exp\left[-\frac{(\ln(OPD_{rms}) - m)^2}{2s^2}\right] \quad (28)$$

where  $m$  is the temporal mean and  $s$  is the temporal standard deviation of the natural log of  $OPD_{rms}(t)$ . The dashed lines in Figure 27 are log-normal distributions where the  $m$  and  $s$  parameters have been calculated from the experimental data at each Mach number. As these curves show, the log-normal distribution captures the general shape characteristics of the experimental data quite well.

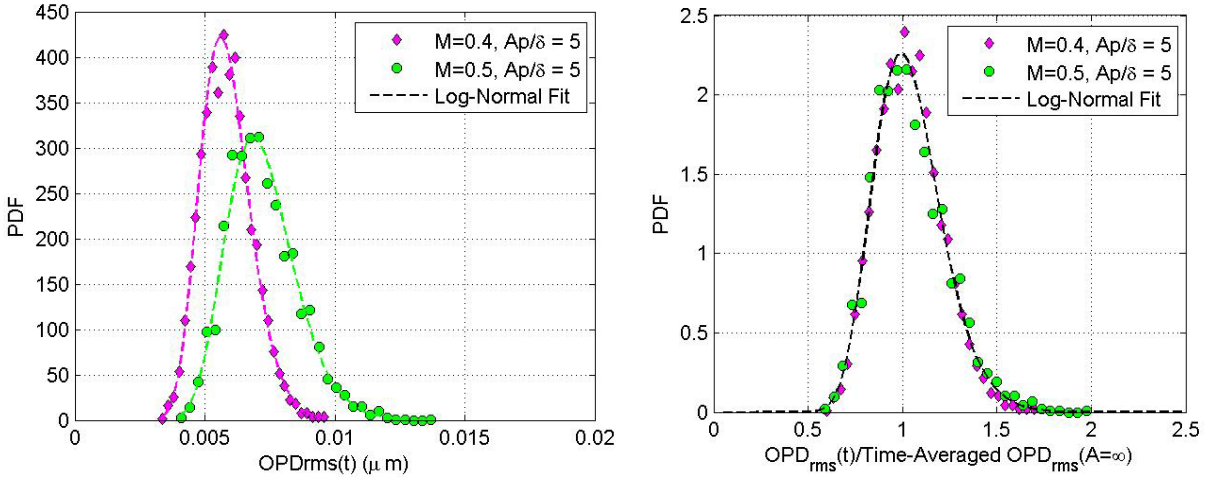


**Figure 27. Left: PDF of  $OPD_{rms}(t;Ap)$ . Right: PDF of the normalized  $OPD_{rms}(t;Ap)/OPD_{rms}(Ap = \infty)$ .  $M = 0.4$  and  $0.5$ .**

Let us define a normalized, aperture-dependent wavefront as

$$OPD_{rms}^{norm}(x,t;Ap) = \frac{OPD(x,t;Ap)}{OPD_{rms}(Ap = \infty)},$$

where the wavefront is normalized by the “infinite-aperture”, time-averaged value of the  $OPD_{rms}$ . Probability distributions of the normalized spatial root-mean-square of  $OPD_{rms}^{norm}(x,t;Ap)$ , labeled  $OPD_{rms}^{norm}(t)$ , for  $M = 0.4$  and  $0.5$  for  $Ap = 10\delta$  are shown in Figure 27, right plot. The probability density functions for different Mach numbers are now collapsed into a single curve, but the shape of the curve is a function of the aperture. Changing the size of the aperture results in different values of the mean and standard deviation for the normalized  $OPD_{rms}^{norm}(t)$ . The values of

the temporal mean,  $\mu$ ,  $\mu(Ap) = \frac{OPD_{rms}(Ap)}{OPD_{rms}(Ap = \infty)}$ , and the temporal standard deviation or the spread,

$\Sigma(Ap)$ , of the  $OPD_{rms}^{norm}(t)$  versus the aperture size were calculated from experimental data and are shown in Figure 28 for the  $M = 0.4$  and  $0.5$ . The slight variation between the different data sets is primarily from experimental errors in the estimation of the boundary-layer thickness. The time-averaged value of  $OPD_{rms}(t;Ap)$  monotonically increases with the aperture size and

approaches the “infinite” aperture value of  $\overline{OPD_{rms}(Ap = \infty)}$ ; therefore,  $\mu$  approaches unity when the size of the aperture is increased. From the experimental data it can be observed that this unity value is achieved when the size of the aperture is larger than  $8\delta$ . From the plot of the spread,  $\Sigma$ , of the  $OPD_{rms}^{norm}(t; Ap)$  in Figure 28, bottom plot, the spread initially increases as the aperture size increases, but at approximately  $Ap = 4\delta$ , the value of  $\Sigma$  begins to decrease. The initial increase is the result of the aperture being smaller than the characteristic size of the optically active structures in the boundary layer. The spread continues to increase with increasing the aperture size until several complete optically active structures are within the aperture at a given instance (which occurs at approximately  $4\delta$ ). However, once the aperture is larger than the characteristic size of several optically active structures, the spread of  $OPD_{rms}(t; Ap)$  will decrease. It is anticipated that if the aperture were allowed to continue to increase in size until it was infinitely large, the value of the spread,  $\Sigma$ , would go to zero while the mean value,  $\mu$ , would become one; thus, for an “infinite” aperture, the PDF of  $OPD_{rms}(t)$  would become the delta-function centered at unity. However, as mentioned before, for very large apertures the streamwise variation of the boundary layer should be taken into account and the presented simplified analysis will no longer be valid.

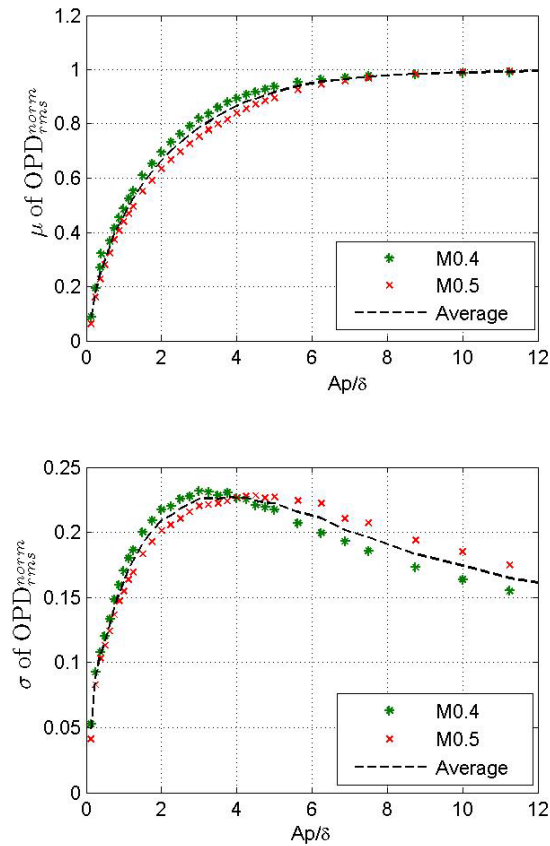


**Figure 28. (Top) The temporal mean,  $\mu$ , and (bottom) the spread,  $\Sigma$ , of  $OPD_{rms}^{norm}(t)$  for different aperture sizes at Mach numbers of 0.4 and 0.5.**

The PDF of the  $OPD_{rms}^{norm}(t)$ , equation (28) can be defined in terms of the mean value,  $\mu$ , and the spread,  $\Sigma$ , which are in turn functions of the aperture size, see Figure 28. These parameters are related to the  $m$  and  $s$  parameters in (28) as,

$$m = \log\left(\frac{\mu}{\sqrt{1 + (\Sigma/\mu)^2}}\right), \quad s^2 = \log\left(1 + (\Sigma/\mu)^2\right) \quad (29)$$

Knowing the PDF of non-dimensional  $OPD_{rms}^{norm}(t)$ , it is possible to reconstruct the actual PDF of *dimensional*  $OPD_{rms}(t)$ , using equations (28) and (29) for any aperture size, using the data from Figure 28 and the scaling law for  $OPD_{rms}(Ap = \infty)$ , equation (EB3).

It is often of interest to find the statistical properties of the instantaneous far-field Strehl Ratio, such as the percentage of time below a certain threshold value, which is directly related to potential data loss for laser-based communication systems [44]. Note that losing the signal for short periods of time does not necessarily mean losing data, as different encoding schemes, such as interleaving or Forward-Error-Correction codes can be employed to send a redundant signal and tolerate a certain data losses, see [44], for instance. Thus, the signal still can be transmitted through a noisy channel, but it will require decoding to make a redundant signal, inevitably increasing amount of data to be transmitted to send the original signal. The knowledge of relative amount of time of intensity drop-outs, drop-out durations and frequencies are helpful in choosing a proper encoding scheme to maximize the *original data* transmission rate.

If a system operates on the absolute value of  $SR(t)$ , the link is presumed to be lost if the absolute value of  $SR(t)$  drops below a prescribed value. Other systems depend on a relative intensity variation,  $SR(t)/\overline{SR(t)}$  and the link is considered to be lost if the relative intensity drops below a certain value. Below we will consider both cases.

#### 4.5.1 Absolute SR threshold

If optical communication systems require that the laser signal strength at the far-field receiving station remains above a minimum value, the communication link can only reliably operate when the Strehl Ratio is above a certain system-defined threshold value,  $TH_{SR}$ . Below this threshold value, the link is considered to be broken.

The Maréchal formula, equation (27), can be rearranged to solve for  $OPD_{rms}$  as a function of  $SR$  as  $OPD_{rms}(t) = \frac{\lambda}{2\pi} \sqrt{-\ln[SR(t)]}$ , or, it can re-written in terms of the  $OPD_{rms}^{norm}(t)$  as,

$$OPD_{rms}^{norm}(t) = \frac{\lambda}{2\pi OPD_{rms}(Ap = \infty)} \sqrt{-\ln[SR(t)]} \quad (30)$$

Using equation (30), the threshold value,  $TH$ , can be found as a function of  $TH_{SR}$ , the laser wavelength,  $\lambda$ , and  $OPD_{rms}(Ap = \infty)$  as,

$$TH = \frac{\lambda}{2\pi OPD_{rms}(Ap = \infty)} \sqrt{-\ln[TH_{SR}]} \quad (31)$$

If the instantaneous value of the normalized  $OPD_{rms}^{norm}$  goes *above* the threshold value,  $TH$ , then the Strehl ratio goes *below*  $TH_{SR}$ , and the optical communication system is considered inoperable and the data are lost. To determine the amount of data lost at the far-field, or, equivalently, the total percentage of time that the normalized  $OPD_{rms}^{norm}(t)$  is above the given

threshold value,  $TH$ , the complementary cumulative distribution function (CCDF) can be used. For the log-normal distribution given by equation (28), the log-normal complementary cumulative distribution function is defined as,

$$CCDF(OPD_{rms}^{norm} > TH) = 1 - \frac{1}{2} \operatorname{erfc}\left(-\frac{\ln(TH) - m}{s\sqrt{2}}\right) \quad (32)$$

where  $\operatorname{erfc}$  is the complementary error function. Figure 29 shows the CCDF, or the percentage of the  $OPD_{rms}^{norm}(t)$  signal above the threshold value,  $TH$ , for different aperture sizes. For example, for the aperture of  $Ap = 10\delta$ , when the threshold value,  $TH$ , is less than 0.5, 100% of the optical aberrations are larger than the threshold value, meaning that in the far field the entire signal will be below the required operational Strehl Ratio threshold and no signal will be registered at the receiver. Increasing the threshold value allows durations of the  $OPD_{rms}^{norm}(t)$  to begin dropping below the threshold,  $TH$ , permitting portions of the signal bit stream to reach the far field with an acceptable Strehl Ratio. For threshold values,  $TH > 1.8$ , none of the normalized  $OPD_{rms}^{norm}(t)$  is above the threshold and the entire signal reaches the far field above the threshold Strehl Ratio. It is important to note that this limitation on  $TH$  is stricter than for energy-deposition systems operating only on the time-averaged intensity on the target.

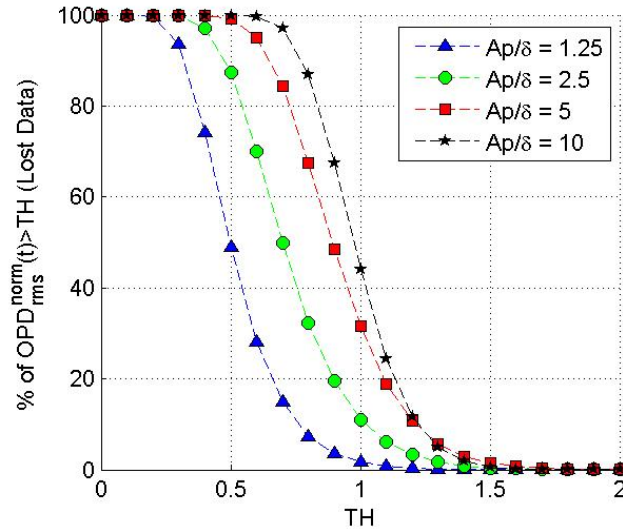


**Figure 29. CCDF of a log-normal PDF showing the percentage of  $OPD_{rms}^{norm}(t)$  that is above the threshold value versus  $TH$  for various aperture sizes.**

Summarizing, the percentage of data lost due to boundary-layer aero-optical aberrations for given flight conditions and the aperture size can be estimated as follows:

1. Calculate  $\overline{OPD_{rms}}(Ap = \infty)$  for the anticipated boundary layer parameters using equation (EB3). The boundary layer thickness can be measured experimentally using a hot-wire, Pitot-probe rake or non-intrusive optical measurements, like the Malley probe [45] or obtained from numerical or other estimations.
2. For a given threshold of Strehl Ratio,  $TH_{SR}$ , determine the threshold value,  $TH$ , for  $\overline{OPD_{rms}}(Ap = \infty)$  and the laser wavelength,  $\lambda$ , using equation (31).
3. For the given  $Ap/\delta$  value, find the mean,  $\mu$ , and the spread,  $\Sigma$ , values from Figure 28.

4. Using equation (29), calculate the  $m$  and  $s$  parameters defining the log-normal distribution of the normalized  $OPD_{rms}^{norm}(t)$ .
5. Calculate the amount of data lost for the given  $m$ ,  $s$ , and  $TH$  parameters using the CCDF( $TH$ ) function, equation (32).

To illustrate the procedure, let us compute the amount data loss for the subsonic boundary layer with the following parameters: the boundary layer thickness of  $\delta = 10$  cm,  $M = 0.8$ , an altitude of 5,000 ft, the viewing angle normal to the wall and the aperture of  $Ap = 5\delta = 0.5$  m. Using Eq. (23), the level of aero-optical distortions would be  $\overline{OPD}_{rms}(Ap = \infty) = 0.11 \mu\text{m}$ . For a laser wavelength of  $\lambda = 1 \mu\text{m}$  and the Strehl Ratio threshold of  $TH_{SR} = 0.5$ , from Eq. (31),  $TH$  can be calculated as 1.2. Finally, Figure 29 gives the relative amount of time when the intensity is below the threshold as 10%.

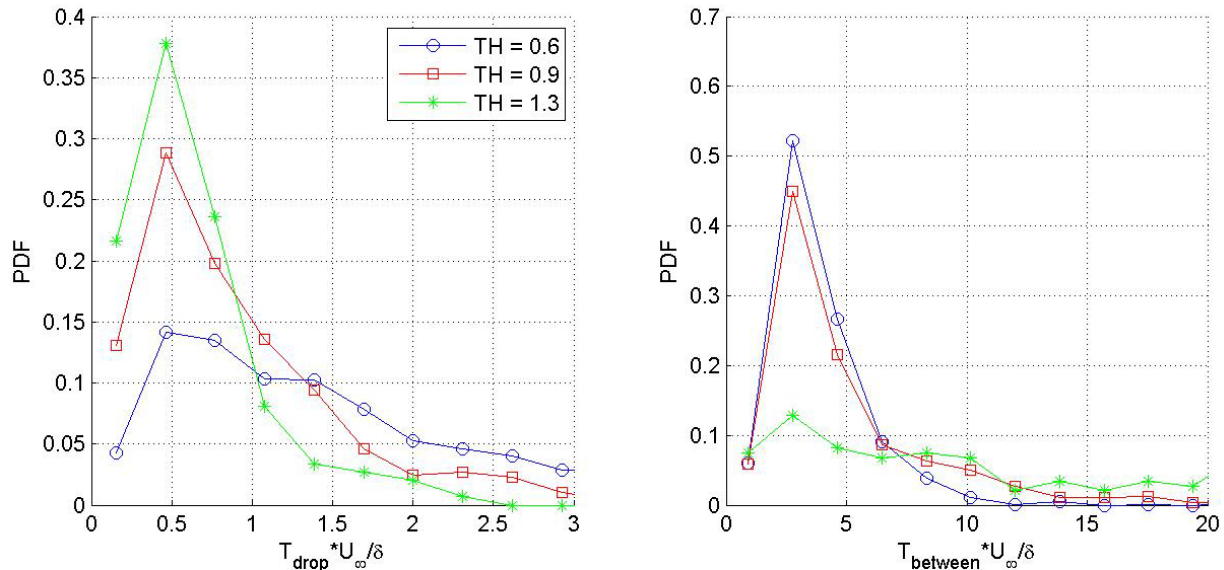


**Figure 30. Probability of the drop-out durations (left) and time interval between successful drop-outs (right) for different threshold values,  $TH$ .**

If the absolute threshold is given, one can also calculate drop-out durations and time intervals between consecutive drop-outs (a relative occurrence of drop-outs). Probability distributions for drop-out durations and times in between drop-outs for the aperture of  $Ap/\delta = 2.0$  for different values of thresholds,  $TH$ , are presented in Figure 30. For the large threshold of  $TH = 1.3$ , the relative amount of the “lost” data is small, about 1%, and the most probable drop-out duration is about  $0.5\delta/U_\infty$ ; the probability distribution for the time interval between drop-outs is wide, indicating intermittent nature of drop-out events, with the average time interval between drop-outs of  $20\delta/U_\infty$ . When the threshold is decreased to  $TH = 0.9$ , the amount of “lost” data becomes about 13%. For this threshold, the most probable drop-out duration is still about  $0.5\delta/U_\infty$ , but the probability tail becomes thicker for this lower threshold, indicating a wider range of drop-out durations. The frequency of drop-out events is increased, with the averaged time interval between drop-outs becoming  $4\delta/U_\infty$ . Then the threshold is decreased even further, to  $TH = 0.6$ , it results in “losing” almost 60% of the data, with drop-outs becoming

even longer, as the averaged drop-out duration becomes about  $2\delta/U_\infty$ ; the average time between drop-outs is decreased to  $3\delta/U_\infty$ . As the typical drop-out duration due to the boundary layer is of the order of the  $\delta/U_\infty$ , or, for a typical transonic boundary layer, of the order of a millisecond, it might potentially result in a loss of several Gigabytes of data during the drop-out, thus definitely requiring some sort of interleaving coding scheme to reliably send data through the free-space, laser-based communication channel.

Although the presented analysis is based on the experimental data collected at subsonic speeds of  $M = 0.4$  and  $0.5$ , aero-optical properties of the supersonic boundary layers can be extracted from subsonic data, when properly normalized, as discussed in Section 4.2.2 [45]. Therefore, this analysis should hold for supersonic boundary layers as well.

#### 4.5.2 Relative intensity variation

Optical distortions caused by the beam propagation through atmosphere over long distances result in intensity fluctuations on the target, which are characterized by a relative intensity variation on the target,  $Z = I(t)/\overline{I(t)} = SR(t)/\overline{SR(t)}$ . For the Kolmogorov-type atmospheric turbulence, these fluctuations have a log-normal distribution and usually described by the log-intensity variance,  $\sigma_{\ln Z}^2 = \overline{(\log Z)^2} - (\overline{\log Z})^2$  [3] and, for weak atmospheric fluctuations and a planar wave, approximately becomes the well-known Rytov variance,  $\sigma_{\ln Z}^2 \approx 1.23C_n^2(2\pi/\lambda)^{7/6}L^{11/6}$  [46]. For aero-optical distortions, though, the distribution of the relative intensity variation,  $Z$ , is clearly not a log-normal one, as it follows from Eqs. (27) and (28). Nevertheless, we can still compute the log-intensity variance as a function of the overall level of aero-optical distortions caused by boundary layers,  $\overline{OPD_{rms}(Ap = \infty)}$ , for different apertures as

$$\sigma_{\ln Z}^2 = \left(2\pi\overline{OPD_{rms}(Ap = \infty)}/\lambda\right)^4 \cdot G_A(Ap/\delta), \quad (33)$$

where  $G_A(Ap/\delta) = \exp(4\mu + 4\Sigma^2) \cdot (\exp(4\Sigma^2) - 1)$  accounts for finite-aperture effects. The log-intensity variance as a function of the relative aperture size,  $Ap/\delta$ , and  $\overline{OPD_{rms}(Ap = \infty)}/\lambda$  is presented in Figure 31, left. The log-intensity variance increases with the increasing  $\overline{OPD_{rms}}$  as the 4<sup>th</sup> power of  $\overline{OPD_{rms}}$ , or, recalling Eq. (23), as the 4<sup>th</sup> power of the boundary-layer thickness,  $\delta$ . Also, it is inversely proportional to the 4<sup>th</sup> power of the laser wavelength. Clearly, these functional dependencies for boundary-layer aero-optical-related effects are quite different than for the atmospheric optical effects, expressed in the Rytov variance. In Figure 31, right,  $G_A(Ap/\delta)$  is plotted versus the aperture size.  $G_A(Ap/\delta)$  and, therefore, the log-intensity variance initially increase with the aperture size, reach the maximum around  $Ap/\delta = 5$  and then start decreasing for larger apertures. Again, this behavior is different from atmospheric optical effects, where the log-normal variance monotonically decreases with the aperture size, so-called aperture-averaging effects, see [3,46], for instance.

Knowing the log-intensity variance caused by turbulent boundary layers, we can compare it to the Rytov variance and find the “equivalent additional” distance the laser beam needs to propagate through the atmosphere to have similar intensity scintillations. Using BL parameters from the example in the previous sub-section, the log-intensity variance can be calculated using Eq. (33) as  $\sigma_{\ln Z}^2 = 0.05$ , and, for a moderately-turbulent atmosphere with  $C_n^2 = 10^{-14} \text{ m}^{-2/3}$ , the “equivalent additional” distance is approximately 330 m. The same boundary-layer parameters,

but at a higher Mach number of  $M = 2$ ,  $\sigma_{\ln Z}^2$  becomes 7.1, with the “equivalent additional” distance of more than 5 km.

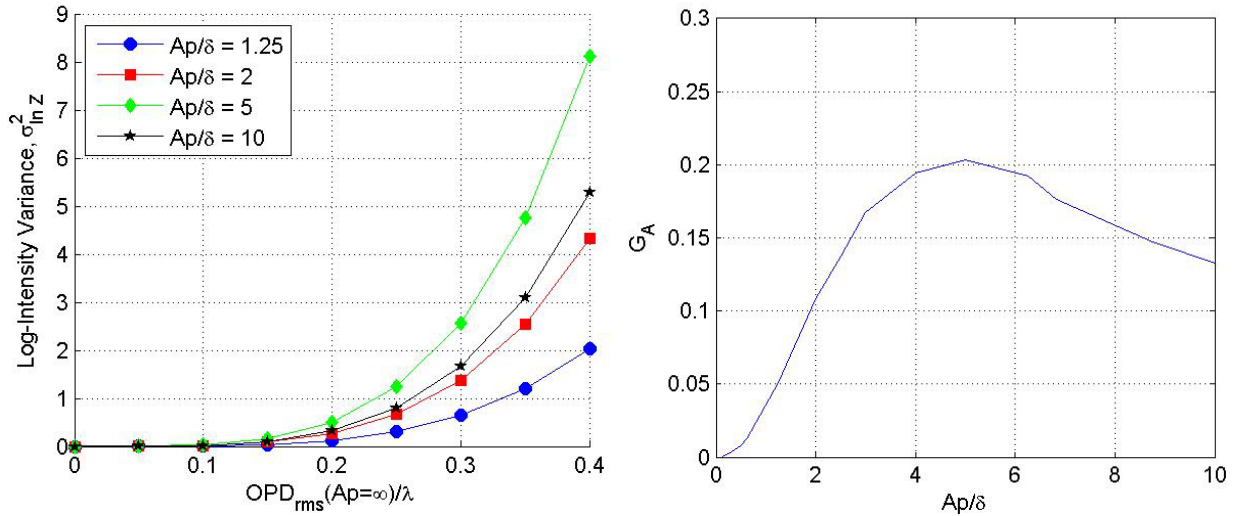


**Figure 31. Left:**  $\sigma_{\ln Z}^2$  as a function of  $OPD_{rms}(Ap = \infty) / \lambda$  for different apertures. **Right:**  $G_A$  as a function of  $Ap/\delta$ .

## 5. Conclusions and Discussion

In this report, the results of extensive systematic experimental investigation of aero-optical distortions caused by compressible subsonic boundary layers using various high-speed wavefront sensors were presented. To measure wavefronts accurately and properly-resolved in time and space, carefully-designed experiments and a suite of sufficiently sensitive, high-bandwidth wavefront sensors and related data reduction procedure were developed to capture instantaneous information necessary to understand the cause of these optical distortions. Careful comparison of results from different sensors helped removing various contamination effects to ensure accurate wavefront measurements for different experimental conditions and provided additional and previously unavailable information about the behavior of aero-optical distortions at low frequencies.

Full characterization of important time-averaged statistical properties of aero-optical distortions, like the mean levels of aero-optical distortions and correlation lengths for different flow speeds, adiabatic and non-adiabatic wall conditions and apertures were measured and analyzed. These quantities describe the optical character of attached turbulent boundary layers and allow studying the statistical character of the structures within the boundary layer that are responsible for aero-optical distortions. The effect of finite aperture size on wavefront statistics and streamwise and spanwise correlation functions have been analyzed and discussed. Based on the empirical curve fit for the spectral behavior of 1-D streamwise wavefronts, analytical prediction demonstrated good agreement with 2-dimensional wavefront data.

In addition to time-averaged statistics, the instantaneous aero-optical aberrations caused by subsonic boundary layers were experimentally investigated for different speeds and aperture sizes and a procedure was developed to determine the percentage of time when the far-field intensity is below a prescribed fixed threshold intensity as a function of given boundary-layer parameters and the laser wavelength. Also, results were used to estimate relative intensity scintillations caused by the boundary layer and it was shown that the aero-optically-related

intensity variations are very different from the ones caused by the atmospheric distortions. Statistics of drop-out intensity, duration and frequency were extracted and important practical tools were developed to quantify negative impact from aero-optical effects on laser-based communication systems. The presented analysis of instantaneous far-field intensity drop-outs has direct implications for communication applications. Performing this analysis on an optical system with given boundary layer conditions would allow a communications engineer to properly size the optical aperture and/or select the appropriate laser wavelength in order to account for additional aero-optical effects caused by boundary layers and achieve an acceptable optical system performance. If the desired performance cannot be achieved due to the boundary layer conditions, then this analysis would dictate how the boundary layer must be altered through active or passive control to mitigate the optical aberration effect of the turbulent boundary layer.

Based on the experimental results, extensive modeling efforts were conducted to predict aero-optical distortions for compressible boundary layers. Large-scale structures were identified as the main source of aero-optical distortions and the correct physical mechanism, the Extended Strong Reynolds Analogy, was identified as the main mechanism responsible for time-averaged aero-optical effects in compressible boundary layers. Using the linking equation, a previously-developed model to predict time-averaged level of subsonic aero-optical distortions was extended to supersonic speeds and was shown to have very good agreement with experimental results in predicting both the level and the convective speed of aero-optical distortions.

Another model was developed and shown to correctly predict experimentally-observed results for cooled/heated boundary layers. This modeling of the turbulent boundary layer led to an important discovery that a mismatch between the wall and the flow temperature can have a profound impact on the magnitude of optical aberrations imprinted on a beam wavefront, as heating the wall could greatly increase the amount of  $OPD_{rms}$  and cooling the wall showed a significant decrease. Several important implications were extracted from this work.

The first implication resulting from the heated wall analysis is the increased availability of low speed turbulent boundary layer facilities to make optical investigations. At low speeds, without heating the underlying wall, the small magnitude of the optical aberrations caused by the turbulent boundary layer render them effectively invisible to modern optical diagnostic instruments, whereas heating the wall can artificially boost the optical aberrations at low velocities, making them detectable to instruments. Further, increasing the wall temperature was shown not to alter the aero-optical structure, but rather it simply amplifies it, meaning that the boundary layer structures and organization of those structures are not significantly altered by the temperature difference, at least in the temperature range tested. This result greatly increases the number and quality of boundary layer facilities that can be used in aero-optic research of the turbulent boundary layer and already led to development of new experimental approaches to study fundamental physics of boundary layers, like the Heated-Wall Boundary-Layer facility at Caltech.

A second implication of the temperature mismatch research relates to real world systems. For an aircraft flying at several kilometers in altitude, the freestream air temperature could be as low as  $-50^{\circ}\text{C}$ . As the aircraft skin might be warmer than the freestream temperature, any optical system propagating through the boundary layer formed around the aircraft will be experiencing a heated wall condition, with the  $\Delta T$  term potentially being quite large. This temperature mismatch must be taken into account in the design of an airborne laser system.

Finally, simply cooling the wall upstream of the optical aperture was shown to significantly mitigate the aero-optical effects, by as much as factor of 5, providing potentially important means to mitigate aero-optical effects.

While the use of suite of different wavefront sensors was shown to be necessary to measure different aspects of aero-optical distortions, this program clearly demonstrated that the Malley Probe provides a valuable tool for investigating the fluid mechanics of turbulent boundary layers cannot be missed. The deflection angle spectra, for example, provide a non-intrusive method of measuring the boundary layer thickness by propagating small-aperture laser beams through and normal to the boundary layer [45]. As long as the walls are reasonably adiabatic and the assumption of a fully-turbulent boundary layer can be made locating the peak in the jitter spectra provides a robust measure of the boundary-layer thickness. Suffice to say, it is clear that the Malley Probe offers a powerful new tool for investigating turbulent boundary layers.

## 6. References

- [1] Gladstone, J. H., Dale, T. P. 1863 “Researches on the Refraction, Dispersion, and Sensitiveness of Liquids”, *Philosophical Transactions of the Royal Society of London*, Vol. **153**, pp. 317-343.
- [2] Gardiner, W.C.Jr, Hidaka, Y. and Tanzawa, T. (1980). “Refractivity of Combustion Gases”, *Combust. and Flame*, **40**, pp. 213-219.
- [3] Tatarski VI. 1961. *Wave Propagation in a Turbulent Medium*. McGraw-Hill, New York, 285 pp.
- [4] Gilbert KG, Otten LJ, editors. *Aero-Optical Phenomena, Progress in astronautics and aeronautics series*, Vol. 80. New York: American Institute of Aeronautics and Astronautics, 1982.
- [5] Jumper, E.J., and Fitzgerald, E.J., “Recent Advances in Aero-Optics,” *Progress in Aerospace Sciences*, **37**, 2001, pp. 299-339.
- [6] Liepmann HW. “Deflection and diffusion of a light ray passing through a boundary layer”, Report SM-14397, Douglas Aircraft Company, Santa Monica Division, Santa Monica, California, May 1952.
- [7] Stine HA and Winovich W. “Light diffusion through high-speed turbulent boundary layers”, Research Memorandum A56B21, NACA, Washington, May 1956.
- [8] G.W. Sutton, “Effects of turbulent fluctuations in an optically active fluid medium”, *AIAA J*, **7** 9 (1969), pp. 1737–1743.
- [9] R.J. Hugo and E.J. Jumper, ”Applicability of the Aero-Optic Linking Equation to a Highly Coherent, Transitional Shear Layer”, *Applied Optics*, **39**(24), pp. 4392-4401, 2000.
- [10] Malley, M. Sutton, G.W. and Kincheloe, N., “Beam-Jitter measurements of turbulent aero-optical path differences,” *Applied Optics*, **31**, pp. 4440-4443, 1992.
- [11] Rose, W.C., “Measurements of Aerodynamic Parameters Affecting Optical Performance,” Air Force Weapons Laboratory Final Report, AFWL-TR-78-191, May 1979.
- [12] Gilbert, K.G., “KC-135 Aero-Optical Boundary-Layer/Shear-Layer Experiments,” *Aero-Optical Phenomena*, Eds. K.G. Gilbert and L.J. Otten, Vol. 80, *Progress in Astronautics and Aeronautics*, AIAA, New York, 1982, pp. 306-324.
- [13] Masson, B., J. Wissler, and L. McMackin, “Aero-Optical Study of a NC-135 Fuselage Boundary Layer,” AIAA Paper 94-0277, January 1994.
- [14] Sutton, G.W., “Aero-Optical Foundations and Applications, *AIAA Journal*, Vol. **23**, pp. 1525-1537, 1985.
- [15] Smith, W.J., *Modern Optical Engineering: The Design of Optical Systems*, McGraw-Hill, NY, 1966, Chap. 3, pp. 49-71.
- [16] S. Gordeyev, E. Jumper, T. Ng and A. Cain, "Aero-Optical Characteristics of Compressible, Subsonic Turbulent Boundary Layer", 34th AIAA Plasmadynamics and Lasers Conference, Orlando, Florida, 23-26 June, 2003, AIAA Paper 2003-3606.
- [17] D. Wittich, S. Gordeyev and E. Jumper, “Revised Scaling of Optical Distortions Caused by Compressible, Subsonic Turbulent Boundary Layers”, 38th AIAA Plasmadynamics and Lasers Conference, Miami, Florida, 25-28 June, 2007, AIAA Paper 2007-4009.

- [18] C. Wyckham, and A. Smits, "Aero-Optic Distortion in Transonic and Hypersonic Turbulent Boundary Layers", *AIAA Journal*, **47**(9), pp. 2158-2168, 2009.
- [19] Morkivin, M.V., 1962, "Effects of compressibility on turbulent flows", in *Mechanique de la Turbulence* (ed. By A. Favre), CNRS, pp. 367-380, Paris, France.
- [20] C. R. Truman and M. J. Lee, "Effects of Organized turbulence structures on the phase distortions in a coherent optical beam propagating through a turbulent shear layer", *Phys. Fluids*, **2**(5), 1990, pp. 851-857.
- [21] C.R. Truman, "The Influence of Turbulent Structure on Optical Phase Distortion Through Turbulent Shear Layer", AIAA Paper 92-2817, January 1992.
- [22] E. Tromeur, E. Garnier, P. Sagaut and C. Basdevant, "LES of Aero-Optical effects in turbulent boundary layer", in *Engineering Turbulence Modelling and Experiments 5: Proceedings of the 5th International Symposium on Engineering Turbulence Modelling and Measurements, Mallorca, Spain, 16-18 September 2002*, Eds. W. Rodi and N. Fueyo, Elsevier Science Ltd, 2002, pp. 327-336.
- [23] Tromeur, E., Garnier, E., Sagaut, P., Basdevant, C., "Large eddy simulations of aero-optical effects in a turbulent boundary layer," *Journal of Turbulence*, Vol. **4**, 2003.
- [24] E. Tromeur, E. Garnier and P. Sagaut, "Large-Eddy Simulation of Aero-Optical Effects in a Spatially Developing Turbulent Boundary Layer", *Journal of Turbulence*, **7**(1), 2006, pp. 1-27.
- [25] Deron, R., Tromeur, E., Aupoix, B., and Desse, J. M., 2002, "Rapport d'Activités 2001 du Project de Recherche Fédérateur Effets Aéro-Optiques," No. RT 4/06008 DOTA, ONERA, France.
- [26] Cress JA. 2010. *Optical aberrations caused by coherent structures in a subsonic, compressible, turbulent boundary layer*. Ph.D. Thesis, Univ. of Notre Dame, Notre Dame, IN
- [27] Nagib, H.M. and Chauhan, K.A., "Scaling of High Reynolds Number Turbulent Boundary Layers Revisited," AIAA Paper 2005-4810, June, 2005.
- [28] Gordeyev, S., Duffin, D., and Jumper, E.J., "Aero-Optical Measurements Using Malley Probe and High- Bandwidth 2-D Wavefront Sensors," *International Conference on Advanced Optical Diagnostics in Fluids, Solids, and Combustion*, Tokyo, Japan (2004).
- [29] De Lucca, N., Gordeyev, S., and Jumper, E.J., "The Study of Aero-Optical and Mechanical Jitter for Flat Window Turrets," AIAA Paper 2012-0623, (2012).
- [30] Schlichting, H., *Boundary-Layer Theory*, 7<sup>th</sup> Ed., McGraw-Hill, Inc., New York & St. Louis, 635-647, (1979).
- [31] Smith AE, Gordeyev S and Jumper E, "Recent Measurements of Aero-Optical Effects Caused by Subsonic Boundary Layers", Acquisition, Tracking, Pointing, and Laser Systems Technologies XXVI, *Proceedings of SPIE*, Volume **8395**, Paper 8395-11, June, 2012.
- [32] Wang K and Wang M, "Aero-optical analysis of turbulent boundary layer and separated shear layer using large-eddy simulation", Acquisition, Tracking, Pointing, and Laser Systems Technologies XXVI, *Proceedings of SPIE*, Volume **8395**, Paper 8395-12, June, 2012.
- [33] Siegenthaler, J.P. (2008) *Guidelines for adaptive-optic correction based on aperture filtration*, PhD thesis, University of Notre Dame.

- [34] Abado, S., Gordeyev, S., and Jumper, E.J., "AAOL Wavefront Data Reduction Approaches", Acquisition, Tracking, Pointing, and Laser Systems Technologies XXVI, Proceedings of SPIE, Volume **8395**, Paper 8395-9, June, (2012).
- [35] Smits, A.J and Dussauge, J.-P., *Turbulent Shear Layers in Supersonic Flow*, American Institute of Physics, Woodbury, New York, 1996.
- [36] Spina, E.F., Smits, A.J., and Robinson, S.K., "The Physics of Supersonic Turbulent Boundary Layers," *Annual Review of Fluid Mechanics*, Vol. 26, 1994, pp. 287-319.
- [37] Morinishi, Y., Tamano, S., and Nakabayashi, K., "Direct numerical simulation of compressible turbulent channel flow between adiabatic and isothermal walls," *Journal of Fluid Mechanics*, Vol. 502, 2004, pp. 273-308.
- [38] Rani, S.L., Smith, C.E., and Nix, A.C., "Boundary-Layer Equation-Based Wall Model for Large-Eddy Simulation of Turbulent Flows with Wall Heat Transfer," *Numerical Heat Transfer, Part B*, Vol. 55, 2009, pp. 91-115.
- [39] Rose, W.C. and Johnson, E.A., "Unsteady Density and Velocity Measurements in the 6 x 6 ft Wind Tunnel", *Progress in Astronautics and Aeronautics: Aero-Optical Phenomena*, Vol. **80**, edited by K. Gilbert and L.J. Otten, AIAA, New York, pp. 218-232, 1982.
- [40] Wang, K. and Wang, M., "Aero-optics of subsonic turbulent boundary layers," *Journal of Fluid Mechanics*, Vol. 696, pp. 122-151, 2012.
- [41] Mahajan V. 1983. Strehl ratio for aberration in terms of their aberration variance. *Journal of the Optical Society of America*, **73**(6), pp.860–861
- [42] Ross TS. 2009. Limitations and applicability of the Maréchal approximation. *Applied Optics*, **48**(10), pp.1812–1818
- [43] Cress, J.A., Gordeyev, S., Post, M.L., and Jumper, E.J., "Aero-Optical Measurements in a Turbulent, Subsonic Boundary Layer at Different Elevation Angles," 39<sup>th</sup> AIAA *Plasmadynamics and Lasers Conference*, AIAA-2008-4214, Seattle, WA, 23-26 June 2008.
- [44] Majumdar AK and Ricklin JC. 2008. *Free-Space Laser Communications: Principles and Advances*, *Optical and Fiber Communications Reports*, Vol. **2**, Springer, 417 pp.
- [45] S. Gordeyev, E. Jumper and T. Hayden, 2012, Aero-Optical Effects of Supersonic Boundary Layers. *AIAA Journal*, Vol. **50**, No. 3, pp. 682-690.
- [46] Andrews LC, Phillips RL and Hopen CY. 2001. *Laser Beam Scintillation with Applications*. SPIE Press.

## Appendix

### List of Publications Based in Whole or in Part on Results from the Current Program

#### Journal Publications

1. S. Gordeyev, J.A. Cress and E.J. Jumper, "Aero-Optical Properties of Subsonic, Turbulent Boundary Layers", submitted to *Journal of Fluid Mechanics*, 2012.
2. S. Gordeyev, J. A. Cress and E.J. Jumper, "Far-Field Laser Intensity Drop-Outs Caused by Turbulent Boundary Layers", to appear in *Journal of Directed Energy*, 2012.
3. S.Gordeyev, E. Jumper and T. Hayden, "Aero-Optical Effects of Supersonic Boundary Layers," *AIAA Journal*, Vol. 50, No. 3, pp. 682-690, 2012.
4. M. Weng, A.Mani and S. Gordeyev, "Physics and Computation of Aero-Optics", *Annual Review of Fluid Mechanics*, Vol. 44, pp. 299-321, 2012.

#### Conference Papers

1. A. Smith, S. Gordeyev and E. Jumper, "Aperture Effects on Aero-Optical Distortions Caused by Subsonic Boundary Layers", 43rd AIAA Plasmadynamics and Lasers Conference, 25 - 28 June 2012, New Orleans, Louisiana, AIAA Paper 2012-2986
2. Smith, AE, Gordeyev, S and Jumper, E, "Recent Measurements of Aero-Optical Effects Caused by Subsonic Boundary Layers", Acquisition, Tracking, Pointing, and Laser Systems Technologies XXVI, Proceedings of SPIE, Volume 8395, Paper 8395-11, June, 2012. (invited paper)
3. A. Smith, S. Gordeyev and E. Jumper, "Aero Optics of Subsonic Boundary Layers over Backward Steps", 42nd AIAA Plasmadynamics and Lasers Conference, 27 - 30 June 2011, Honolulu, Hawaii, AIAA Paper 2011-3277.
4. S.Gordeyev, J. Cress and E. Jumper, "Far-Field Intensity Drop-Outs Caused by Turbulent Boundary Layers", DEPS, Beam Control Conference, 23-26 May, 2011, Orlando, FL. Paper 11-BC-050
5. S. Gordeyev, E. Jumper and T. Hayden, "Aero-Optics of Supersonic Boundary Layers", 49th Aerospace Science Meeting and Exhibit, Orlando, Florida, 4-7 Jan, 2011, AIAA Paper 2011-1325.
6. S. Gordeyev, D. Wittich and E. Jumper, "Aero-Optical Issues for Free-Space Communication", invited paper for Beam Control Conference, 5<sup>th</sup> Directed Energy Systems Symposium, Monterey, CA, 12-16 Apr, 2010.
7. J. Cress, S. Gordeyev and E. Jumper "Aero-Optical Measurements in a Heated, Subsonic, Turbulent Boundary Layer", 48th Aerospace Science Meeting and Exhibit, Orlando, Florida, 4-7 Jan, 2010, AIAA Paper 2010-0434.